Monthly Notices of the ROYAL ASTRONOMICAL SOCIETY

MNRAS **528,** 6193–6209 (2024) https://doi.org/10.1093/mnras/stae396
Advance Access publication 2024 February 7

Collisions of red giants in galactic nuclei

Taeho Ryu [1,2]★ Pau Amaro Seoane,[3,4,5,6] Andrew M. Taylor[7] and Sebastian T. Ohlmann[8]

[1]*Max Planck Institute for Astrophysics, Karl-Schwarzschild-Str 1, D-85748 Garching, Germany*
[2]*Physics and Astronomy Department, Johns Hopkins University, Baltimore, MD 21218, USA*
[3]*Institute of Multidisciplinary Mathematics, Universitat Politècnica de València, Universitat Politècnica de València, València, 46022, Spain*
[4]*Max Planck Institute for Extraterrestrial Physics, Garching, 85748, Germany*
[5]*Higgs Centre for Theoretical Physics, Edinburgh, EH9 3FD, UK*
[6]*Kavli Institute for Astronomy and Astrophysics, Beijing 100871, China*
[7]*DESY, Zeuthen, 15738, Germany*
[8]*Max Planck Computing and Data Facility, Garching, 85748, Germany*

Accepted 2024 January 26. Received 2024 January 25; in original form 2023 July 14

ABSTRACT

In stellar-dense environments, stars can collide with each other. For collisions close to a supermassive black hole (SMBH), the collisional kinetic energy can be so large that the colliding stars can be destroyed, potentially releasing an amount of energy comparable to that of a supernova. These black hole-driven disruptive collisions have been examined mostly analytically, with the non-linear hydrodynamical effects being left largely unstudied. Using the moving-mesh hydrodynamics code AREPO, we investigate high-velocity ($>10^3$ km s^{-1}) collisions between 1 M$_\odot$ giants with varying radii, impact parameters, and initial approaching velocities, and estimate their observables. Very strong shocks across the collision surface efficiently convert $\gtrsim$10 per cent of the initial kinetic energy into radiation energy. The outcome is a gas cloud expanding supersonically, homologously, and quasi-spherically, generating a flare with a peak luminosity $\simeq 10^{41}$–10^{44} erg s^{-1} in the extreme ultraviolet band ($\simeq$10 eV). The luminosity decreases approximately following a power law of $t^{-0.7}$ initially, then $t^{-0.4}$ after $t \simeq 10$ d at which point it would be bright in the optical band ($\lesssim$1eV). Subsequent, and possibly even brighter, emission would be generated due to the accretion of the gas cloud on to the nearby SMBH, possibly lasting up to multiyear time-scales. This inevitable BH–collision product interaction can contribute to the growth of BHs at all mass scales, in particular, seed BHs at high redshifts. Furthermore, the proximity of the events to the central BH makes them a potential tool for probing the existence of dormant BHs, even very massive ones which cannot be probed by tidal disruption events.

Key words: hydrodynamics – stars: kinematics and dynamics – Galaxy: nucleus – quasars: supermassive black holes – Transients.

1 INTRODUCTION

Dynamical interactions between stars in stellar-dense environments, e.g. globular clusters and galactic centres, play a crucial role in driving the evolution of the host and determining its thermodynamic state (Hut et al. 1992). If the stellar density is sufficiently high, stars can collide with relative velocities comparable to the dispersion velocity of the host. In globular clusters, up to 40 per cent of main-sequence stars in the core would undergo a collision during the lifetime of the cluster (Hills & Day 1976). For clusters with very high number densities ($\gtrsim 10^7$ pc^{-3}), a star may suffer multiple such collisions (Dale & Davies 2006).

Galactic centres are extreme environments where stars are densely packed (e.g. 10^6–10^7 pc^{-3} for nuclear clusters; Neumayer, Seth & Böker 2020, and references therein) around a supermassive black hole (SMBH). Because the relative velocity between stars near the SMBH is roughly the Keplerian speed[1] $\propto r^{-0.5}$, stars near the BH would collide at very high speeds (e.g. $v_{\rm rel} \gtrsim 2000$ km s^{-1} within $\simeq$0.1 pc around a 10^7 M$_\odot$ BH). If the kinetic energy of the collision ($\gtrsim 10^{50}$ erg for a collision between two stars with mass $M_\star = 1$ M$_\odot$ and $v_{\rm rel} \gtrsim 2000$ km s^{-1}) is greater than the binding energy of the stars (10^{48}–10^{49} erg for $M_\star = 1$ M$_\odot$), the stars would be destroyed, leaving behind an expanding gas cloud. If even a small fraction of the collisional kinetic energy is converted into radiation, the high-velocity collision can generate a bright electromagnetic transient from the galactic nucleus region.

The total rates of such events between main-sequence stars have been estimated to be 10^{-4} to 10^{-5} yr^{-1} galaxy^{-1} (Rose et al. 2020, 2023; Amaro Seoane 2023b) if the core is fully relaxed to the Bahcall–Wolf density power law $\propto r^{-7/4}$ (Bahcall & Wolf 1976).[2] The

[1]Sellgren et al. (1990) observed a decrease in the CO absorption line strength in the central region of our Galaxy, confirming that the velocity dispersion of stars increases towards the centre.
[2]While the Bahcall–Wolf solution is a mathematically correct solution when all stars have the same mass, in the realistic situation where the stellar-

★ E-mail: tryu@mpa-garching.mpg.de

© 2024 The Author(s).
Published by Oxford University Press on behalf of Royal Astronomical Society. This is an Open Access article distributed under the terms of the Creative Commons Attribution License (https://creativecommons.org/licenses/by/4.0/), which permits unrestricted reuse, distribution, and reproduction in any medium, provided the original work is properly cited

Downloaded from https://academic.oup.com/mnras/article/528/4/6193/7603392 by Deutsches Elektronen Synchrotron DESY user on 18 December 2024

rate for collisions between giants could be higher due to larger cross-sections (Amaro Seoane 2023b). However, if collisions continuously deplete the inner part of the stellar-density cusp, the rate would become smaller, e.g. $\simeq 10^{-5}$ to 10^{-7} yr^{-1} galaxy^{-1} for main-sequence stars, depending on the assumption of the stellar influx into the centre (Balberg & Yassur 2023). Since these powerful collisions essentially destroy stars in galactic centre environments, these events can affect the frequency of other types of nuclear transients. For example, Balberg & Yassur (2023) suggest that high-velocity collisions can almost completely suppress extreme mass-ratio inspirals.

High-velocity collisions between main-sequence stars (e.g. Benz & Hills 1987, 1992; Lai, Rasio & Shapiro 1993; Rauch 1999; Freitag & Benz 2005) have been studied using numerical simulations, focusing on the mass ejection and the impact of such collisions on the thermodynamic state of the host, rather than their observation signatures. Observational signatures of the electromagnetic radiation from such collisions have been studied mostly analytically. For example, Balberg, Sari & Loeb (2013) showed that two stars in a compact binary can collide at high speed when passing very close to an SMBH, which can generate a flare as bright as supernovae. Recently, Amaro Seoane (2023b) analytically investigated the observables of high-velocity collisions between stars of various types in galactic nuclei. They found that the peak luminosity of high-velocity collisions can be as high as $10^{44}\eta_{\rm rad}$ erg s^{-1}. Here, $\eta_{\rm rad}$ is one of the determining factors which measures how efficiently the initial kinetic energy is converted into radiation energy. If $\eta_{\rm rad}$ is of order unity, the peak luminosity can be comparable to different types of nuclear transients, such as tidal disruption events. However, $\eta_{\rm rad}$ in their work was left as a free parameter because evaluating $\eta_{\rm rad}$ involves non-linear hydrodynamics effects such as shocks, which cannot be done analytically.

In this paper, we investigate the hydrodynamics of high-velocity collisions between 1 $M_\odot$ giants and numerically estimate the radiation conversion efficiency and their observables, using the moving-mesh hydrodynamics code AREPO (Springel 2010; Pakmor et al. 2016; Weinberger, Springel & Pakmor 2020). In the simulations, we consider collisions with $v_{\rm rel} = 10^4$ km s^{-1} between two identical 1 $M_\odot$ giants with four different radii ($R_\star = 10$, 20, 50, and 100 $R_\odot$), four impact parameters ($b = 0.04\,R_\star$, $0.2\,R_\star$, $0.4\,R_\star$, and $0.8\,R_\star$), and three initial approaching velocity ($v_{\rm rel} = 10^4$, 5×10^3, and 2.5×10^3 km s^{-1}). The largest approaching speed corresponds to roughly the largest relative velocity for stellar collisions near the BH, i.e. the Keplerian velocity at the smallest possible distance from the BH where at least two stars exist for a typical stellar density around a massive BH assuming the Bahcall–Wolf power law: $r \simeq 10^{-5}$ pc for 10^5 $M_\odot$ BH, $\simeq 10^{-4}$ pc for 10^6 $M_\odot$ BH, and $\simeq 10^{-3}$ pc for 10^7 $M_\odot$ BH. Because collisions with lower relative velocities are expected to create fainter transients, our simulations with the largest $v_{\rm rel}$ would provide an upper limit for the luminosity and total radiated energy of these events.

This paper is organized as follows. We describe our methods in Section 2, including the code description (Section 2.1), stellar models (Section 2.2), and initial conditions (Section 2.3). Then, we present our results in Section 3 and discuss astrophysical implications for the collisions in Section 4. Finally, we summarize and conclude in Section 5.

mass distribution is inhomogeneous, the slope can be steeper (Alexander & Hopman 2009; Preto & Amaro-Seoane 2010).

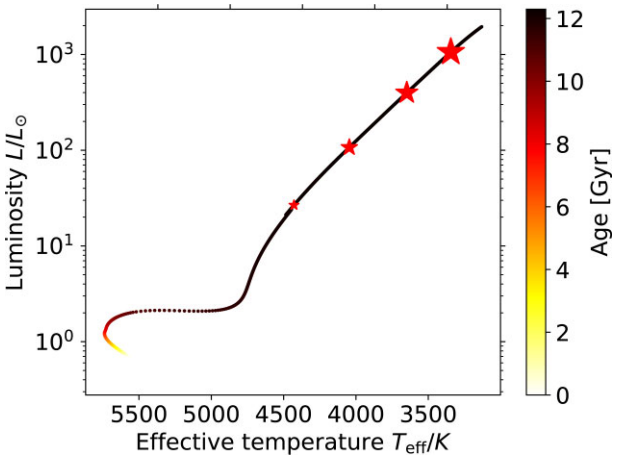

Figure 1. Evolution of a 1 $M_\odot$ star in a Hertzsprung–Russell diagram. The colour bar shows the age of the star. The four star symbols mark the four giant models adopted for collision experiments: (from smallest to largest symbols) $R_\star \simeq 9$, 20, 50, and 100 $R_\odot$.

2 METHODS

2.1 Code

We perform a suite of 3D hydrodynamics simulations of high-velocity collisions between red giants using the massively parallel gravity and magnetohydrodynamics moving-mesh code AREPO (Springel 2010; Pakmor et al. 2016; Weinberger et al. 2020). The code inherits advantages of the two widely used hydrodynamical schemes, the Lagrangian smoothed particle method and the Eulerian finite-volume method, allowing for an accurate treatment of supersonic flows and shock capturing without introducing an artificial viscosity and low advection errors. We use the ideal equation of states that takes into account radiation pressure assuming local thermodynamic equilibrium,

$$P = \frac{\rho k_{\rm B} T}{\mu m_{\rm p}} + \frac{4\sigma}{3c} T^4, \tag{1}$$

where P is the total pressure, ρ the density, $k_{\rm B}$ the Boltzmann constant, T the temperature, $\mu = 0.62$ the mean molecular weight, $m_{\rm p}$ the proton mass, and σ the Stefan–Boltzmann constant.

2.2 Stellar model

We adopt the internal structure of giants evolved using the 1D stellar evolution code MESA (version r22.05.1; Paxton et al. 2011, 2013) to model giants in 3D. The star has an initial mass $M_\star = 1\,M_\odot$ and a metallicity of $Z = 0.02$. We treat the mixing processes and winds following Choi et al. (2016). More specifically, we model convection using the mixing length theory with a mixing length parameter of 1.81. We adopt the Ledoux (1947) criterion to determine the boundary of the convective regions and the exponential overshoot prescription (Herwig 2000) with parameters $f = 0.016$, $f_0 = 0.008$ at the top of the core and $f = 0.0174$, $f_0 = 0.0087$ at the bottom of the hydrogen-burning shell. Semiconvection is treated following Langer, Fricke & Sugimoto (1983) with an efficiency factor of 0.1. We allow the star on the red giant branch to lose mass via wind following the prescription from Reimers (1975) with scaling factor of 0.1.

Fig. 1 shows the evolution of the 1 $M_\odot$ star in a Hertzsprung–Russell diagram until it reaches the tip of the red giant branch. We take the giants at four different evolutionary stages where their radii

Downloaded from https://academic.oup.com/mnras/article/528/4/6193/7603392 by Deutsches Elektronen Synchrotron DESY user on 18 December 2024

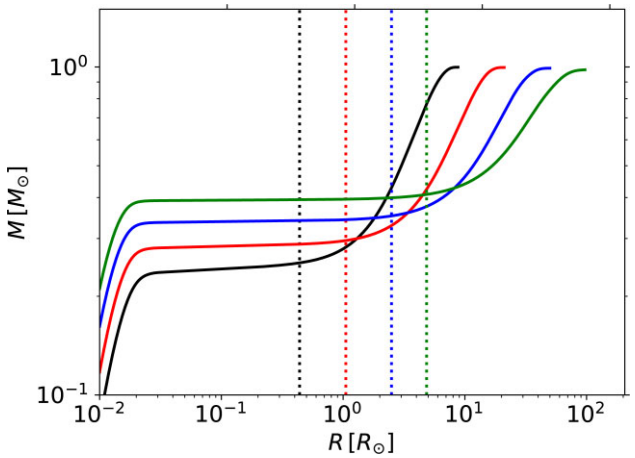

Figure 2. Enclosed mass as a function of radius for the four giants with $R_\star = 10\,\mathrm{R}_\odot$ (black), $20\,\mathrm{R}_\odot$ (red), $50\,\mathrm{R}_\odot$ (blue), $100\,\mathrm{R}_\odot$ (green). The vertical dotted lines, sharing the same colour, indicate the size of the region modelled using a point particle. Although the point particle size is greater than the size of the core ($R \simeq 0.02\,\mathrm{R}_\odot$), given the flat mass–radius relation between the core radius and the point particle radius, we essentially retain the total energy budget inside the star above the core with significantly low computational costs.

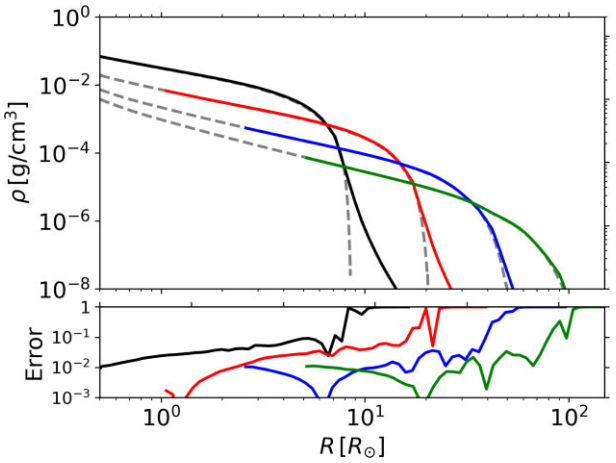

Figure 3. The radial density profile (*top*) of the giants with four different radii relaxed for 5–10 stellar dynamical times and the relative error with respect to the MESA models (*bottom*), as a function of radius from the core. The dashed grey lines in the *top* panel show the density profiles of the MESA models. The density profiles of the 3D stars match well with the MESA models within a few per cent except for those at the stellar surface.

are $R_\star \simeq 10$, 20, 50, and $100\,\mathrm{R}_\odot$ (indicated by the star symbols in the figure).

We construct 3D giants from the 1D giant models using the method developed in Ohlmann et al. (2017) with 10^6 cells. Modelling the entire giant with gas cells is computationally expensive given very steep density gradients. So instead, we model the inner part of the star with a point particle, representing effectively the core. Furthermore, we place gas cells on top of it such that the internal structure above the core matches with the MESA model while the entire star stays in hydrostatic equilibrium. The point particle interacts only gravitationally with gas: it only gravitationally pulls the envelope which is cancelled by the pressure gradient of the gas when the star is in isolation. We choose that the size of the region modelled using a point particle is 5 per cent of the stellar radius ('point particle radius'). The point particle radius is in fact greater than the size of the core ($R \simeq 0.02\,\mathrm{R}_\odot$). This choice is justified by the fact that the mass of the core is effectively the same as the enclosed mass within $\simeq 0.05\,R_\star$ (vertical dotted lines), as illustrated in Fig. 2. This means the total binding energy inside our 3D giants is essentially the same as what we would have had when the point particle radius were exactly the core radius. With this choice of the point radius, while we reduce computational costs significantly, we lose only a small fraction of the total energy budget inside the star.

We then relax the 3D stars fully in isolation, which usually takes 5–10 stellar dynamical times ($\sqrt{R_\star^3/G\,M_\star}$). Fig. 3 shows the radial density of the fully relaxed stars above the point particle (*top* panel) and their errors (*bottom* panel) relative to the MESA models. The relative errors of the density of the inner part of the stars, where most of the mass is concentrated, are less than a few per cent. Although the errors at the surface are relatively large, the deviation of such small masses at the surface, corresponding to the plateau at the end of each line in Fig. 2, should not affect our results.

We performed resolution tests for nearly head-on collisions between giants with $R_\star = 100\,\mathrm{R}_\odot$ with different resolutions. The choice of the collision parameters are motivated by the fact that the impact of the shock in such a collision is the strongest (see Fig. 8), which requires the highest resolution. We first constructed giants with $N = 2.5 \times 10^5$, 5×10^5, 10^6, 2×10^6, and 4×10^6 cells and performed the collision experiments. We find that the results have already converged very well when $N \geq 10^6$: the conversion factor η_{rad}, defined in equation (8), differs by less than 1 per cent. In fact, the difference in η_{rad} between $N \leq 5 \times 10^5$ and $N = 10^6$ is already reasonably small, $\lesssim$20 per cent for $N = 2.5 \times 10^5$ and $\lesssim$10 per cent for $N = 5 \times 10^5$ relative to the case with $N \geq 10^6$. Furthermore, we confirmed that the total energy is conserved within $\lesssim$1 per cent until the end of the simulations.

2.3 Initial conditions

We place two identical stars, initially separated by $10\,R_\star$, on a hyperbolic orbit with some relative velocity at infinity v_{rel}. So it takes $10\,R_\star/v_{\mathrm{rel}} \simeq$ (0.1–1) d, depending on $R_\star$ and v_{rel}, until the two stars collide. We note that the time is measured since collision in this paper: accordingly, the initial time of the simulations is $t \simeq -$(0.1–1) d. Those stars are embedded in a low-density background medium with density of $10^{-18}\,\mathrm{g\,cm^{-3}}$ and temperature of 10^4 K. The background density is comparable to the density of the interstellar medium (ISM) at the Galactic centre ranging between 10^5 and 10^6 particles $\mathrm{cm^{-3}}$ (Gillessen et al. 2019) at Galactic centre distances that dominate the collision rate (see Amaro Seoane 2023b). We discuss the impact of the background density and temperature on the properties of collision products in Section 4.1. Our fiducial model is the near-head-on collision between the two $10\,\mathrm{R}_\odot$ giants initially approaching towards each other at $v_{\mathrm{rel}} = 10^4\,\mathrm{km\,s^{-1}}$ with an impact parameter $b = 0.04\,R_\star$. Here, $b = 0.04\,R_\star$ is the smallest possible impact parameter given the softening length of the point particle: in other words, the gravity of the point particles becomes inaccurate at the closest approach distance with $b < 0.04\,R_\star$. For this giant, we additionally consider off-axis collisions with larger impact parameters, $b = 0.2$, 0.4, and $0.8\,R_\star$, and two additional $v_{\mathrm{rel}} = 2500$ and 5000 $\mathrm{km\,s^{-1}}$, to study the dependence of the impact parameter and the collision velocity, respectively. For larger giants, we only consider the near-head-on collisions with $v_{\mathrm{rel}} = 10^4\,\mathrm{km\,s^{-1}}$. The initial parameters of the models are summarized in Table 1.

Downloaded from https://academic.oup.com/mnras/article/528/4/6193/7603392 by Deutsches Elektronen Synchrotron DESY user on 18 December 2024

Table 1. Initial parameters: (from left to right) model number, stellar mass, stellar radius, relative velocity $v_{\rm rel}$ at infinity, and impact parameter b.

Model number	Mass $M_\odot$	Radius $R_\odot$	$v_{\rm rel}$ $\times 10^3$ km s^{-1}	Impact parameter b $R_\star$
1	1	10	10	0.04
2	1	10	10	0.2
3	1	10	10	0.4
4	1	10	10	0.8
5	1	10	5	0.04
6	1	10	2.5	0.04
7	1	20	10	0.04
8	1	50	10	0.04
9	1	100	10	0.04

3 RESULT

3.1 Overview

We provide an overview of the evolution of the collision product using our fiducial model, e.g. head-on collision between the two $10\,R_\odot$ giants. We present in Fig. 4 (from *top* to *bottom*) the density ρ, the temperature T, the Mach number $\mathcal{M}$, and the speed in the mid-plane at four different times in our fiducial model.

Initially, the two stars approach at $v_{\rm rel} \simeq 10^4$ km s^{-1} (first column). Since their first contact, the envelopes are continuously compressed due to the converging motion. Along the contact surface (the pronounced narrow feature across the centre in the second column, dubbed 'shock surface'), pressure gradients are built up and the temperature is raised above 10^7 K due to adiabatic compression. As the later incoming gas collides supersonically with the pressure wall, shocks are created. Some of the very hot gas in the shock surface escapes radially perpendicular to the collision axis (or along the shock surface) with an opening angle of $\simeq 30^\circ$ and speeds of a few thousands km s^{-1}, which is not particularly high compared to the rest. At the strongest compression, a significant fraction of the kinetic energy is converted into heat energy ($\gtrsim$30 per cent), which is already a few orders of magnitude greater than the total binding energy of the stars. When the pressure gradient exceeds the ram pressure, the compressed gas bounces off and expands quasi-spherically and homologously at supersonic speeds (see third and fourth column panels in Fig. 4). On top of the expanding motion, the converted heat energy continuously drives the outer part of the gas cloud to expand by the PdV work, meaning that some of the heat energy is converted back into kinetic energy. At the same time, the outer edge of the cloud supersonically collides with the background medium. This has two effects. First, mass piles up at the boundary between the gas cloud and the background medium, reducing the kinetic energy of the expansion front. Secondly, shocks are created, which dissipates the kinetic energy of the expansion front to heat energy. As a result of both effects, the expansion front slows down.

3.2 Evolution of expanding cloud – parameter dependence

3.2.1 Fiducial case

To describe the evolution of the expanding gas more quantitatively, we show in Fig. 5 the spherically averaged density ρ and (mass-weighted) temperature T, the expansion speed $v^{\rm r}$, and the area-weighted average of the optical depth τ over the solid angle for our fiducial model as a function of distance from the collision point at five logarithmically sampled times between 1 and 30 d after collision. The density ρ (*top-left*) and the temperature T (*top-right*) of the inner regions of the expanding gas cloud are nearly constant. As the cloud expands adiabatically, the overall level of ρ and T drops while maintaining its slope: $\rho \simeq 10^{-8}$ g cm^{-3} at $t \simeq 1$ d to 10^{-12} g cm^{-3} at $t \simeq 30$ d, and $T \simeq 2 \times 10^5$ K at $t = 1$ d to 5×10^3 K at $t \simeq 30$ d, at which point the cloud is cooler than the background medium. ρ and T outside the flat region decay towards the outer edge with a different steepness: the density drops following a power law of $\propto r^{-\lambda}$ with $\lambda \simeq 12$–13 upon collision, gradually decreasing to $\lambda \simeq 8$ at $t \simeq 30$ d. But the temperature decays rather like $\propto r^{-1}$ at $1 \lesssim t \lesssim 30$ d. The decaying slopes of ρ and T depend on $R_\star$, b, and $v_{\rm rel}$, but the dependence of the slope of T is generally stronger. $\mathrm{d}\ln\rho/\mathrm{d}\ln r$ is almost the same, independent of $R_\star$ whereas $-\mathrm{d}\ln T/\mathrm{d}\ln r$ tends to be larger for larger $R_\star$ (e.g. $\lambda \simeq 2$–3 for $R_\star = 100\,R_\odot$). $\mathrm{d}\ln T/\mathrm{d}\ln r$ is steeper for larger b (e.g. $\lambda \simeq 2$–3 for $b = 0.8\,R_\star$), while $\mathrm{d}\ln\rho/\mathrm{d}\ln r$ is only slightly less steeper for larger b (e.g. $\lambda \simeq 12$ for $b = 0.8\,R_\star$). The dependence of the slopes on $v_{\rm rel}$ is relatively weak: λ for ρ is almost same for 2500 km s^{-1} $\le v_{\rm rel} \le 10^4$ km s^{-1} and λ for T is slightly larger for smaller $v_{\rm rel}$ (e.g. $\lambda \simeq 1$–1.5 for $v_{\rm rel} = 2500$ km s^{-1}).

As shown in the *bottom-left* panel of Fig. 5, the cloud expands homologously, i.e. $v^{\rm r} \propto r$ or constant $v^{\rm r}$ at the same mass coordinate, which is also found in all other models. Right after the collision, the maximum expansion velocity at the outer edge is greater than the initial relative velocity by a factor of $\simeq$5 and stays constant. The period of time with a constant peak $v^{\rm r}$ is very brief for this particular model ($\lesssim$0.1 d). However, the constant maximum $v^{\rm r}$ phase is longer for collisions with larger $R_\star$, which is illustrated in the *bottom-right* panel of Fig. 6. After the constant maximum $v^{\rm r}$ phase, the peak expansion velocity continuously decreases due to the interactions with the background medium.

The gas cloud is initially optically thick. The optical depth to the centre, estimated using an OPAL opacity table for Solar metallicity (Iglesias & Rogers 1996), is $\tau \gtrsim 10^5$ at $t \simeq 1$ d, as demonstrated in the *bottom-right* panel of Fig. 5. As it expands and cools, τ decreases following a power law of $t^{-7/3}$ (see the *bottom-right* panel of Fig. 6), indicating that the entire cloud will become optically thin within 7–8 months, consistent with the analytical estimate by Amaro Seoane (2023b). The nearly flat τ inside the cloud indicates that the transition from optically thick to completely optically thin may be prompt.

3.2.2 Comparison between models

To further demonstrate the dependence of the stellar radius $R_\star$, the impact parameter b and the initial relative velocity $v_{\rm rel}$, we compare in Fig. 6 the evolution of the same four quantities, shown in Fig. 5 between different models. For a proper comparison, we estimate $\overline{\rho}$ as the average volume within a distance enclosing 75 per cent of the gas mass[3] and $\overline{T}$ as the mass-weighted average of T within the same volume. As shown in the *top* panels, $\overline{\rho}$ and $\overline{T}$ decrease over time, following a power law of t^{-3} and t^{-1}, respectively, almost independently of $R_\star$ and b except for $\overline{T}$ with $v_{\rm rel} = 2.5 \times 10^3$ km s^{-1}. The t^{-3} power law for $\overline{\rho}$ is expected from a homologous expansion: $\rho \propto (v^{\rm r}t)^{-3} \propto t^{-3}$. As the t^{-1}-scaling relation for $\overline{T}$ suggests, the total (radiation + gas) internal energy at a given mass coordinate decreases like t^{-1}.[4] The significant deviation from the t^{-1} power law for $v_{\rm rel} = 2500$ km s^{-1} indicates that there is continuous energy

[3]Note that the radius enclosing 75 per cent of the cloud mass corresponds to the radius inside which ρ and T are constant, coinciding with the distance of the cores from the collision point.

[4]Total specific energy $= 4\sigma T^4/[3c\rho] + k_{\rm B}T/[\mu m_{\rm p}] \propto t^{-1}$ because $T \propto t^{-1}$ and $\rho \propto t^{-3}$.

Downloaded from https://academic.oup.com/mnras/article/528/4/6193/7603392 by Deutsches Elektronen Synchrotron DESY user on 18 December 2024

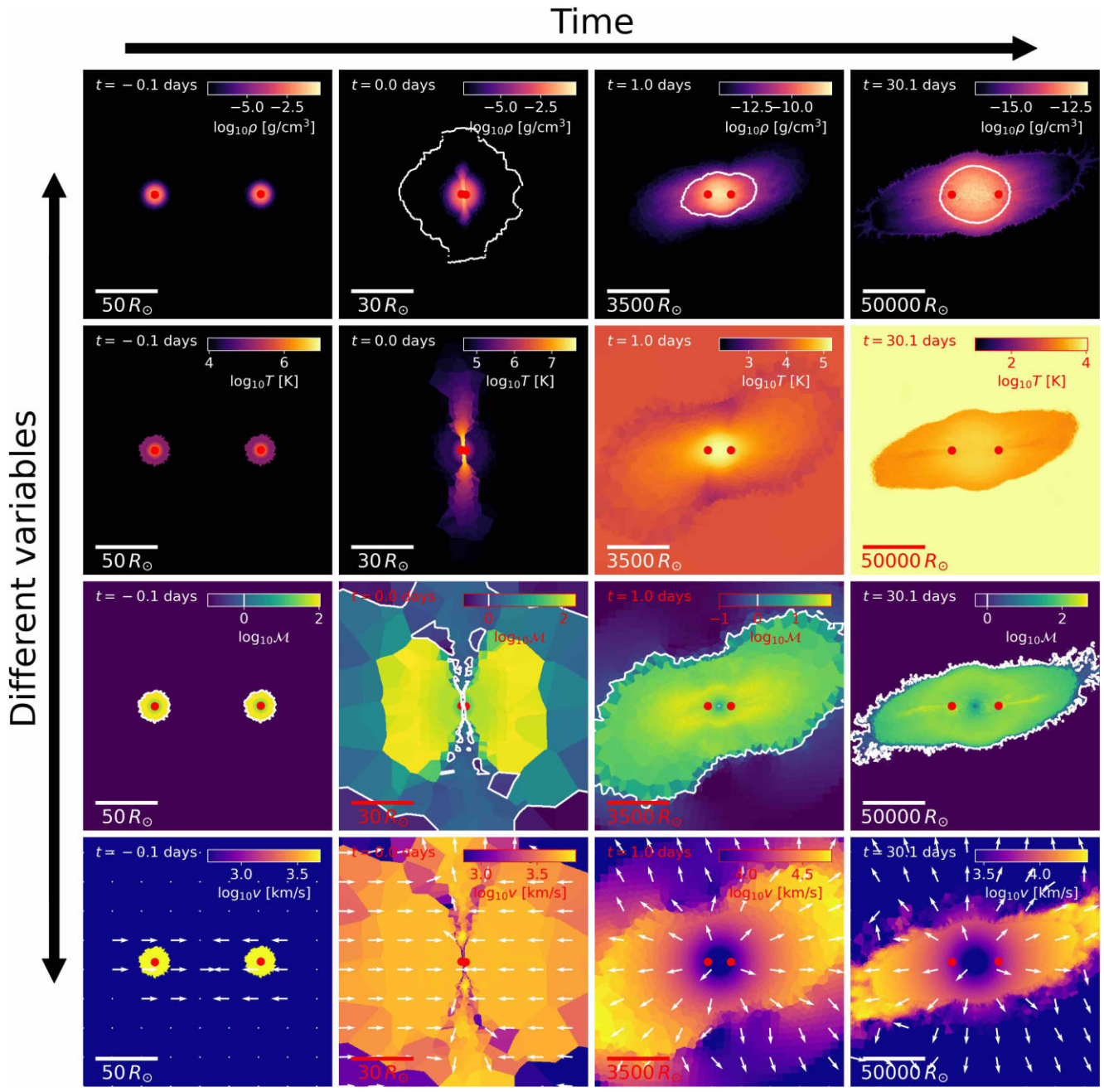

Figure 4. Density ρ (*top*), temperature T (*top-middle*), Mach number $\mathcal{M}$ (*bottom-middle*), and speed v (*bottom*) of gas in a nearly head-on ($b = 0.04R_\star$) collision between two giants with $R_\star = 10\,\mathrm{R}_\odot$ at four different times, $t = -0.07$ d (before collision), 0 d (at collision), 1 and 30 d (after collision). The red dots in each panel indicate the location of the cores. The white contour line in the *top* panel for ρ shows the location of the photosphere at which the radially integrated optical depth $\simeq 1$ and those in the *bottom-middle* panel for $\mathcal{M}$ the boundaries at $\mathcal{M} \simeq 1$. The arrows in the *bottom* panels indicate the direction of gas motion. Initially the two stars start to move towards each other with $v_{\rm rel} = 10^4$ km s^{-1} (*left*). At collision, very steep pressure gradients are built up at the collision surface and strong shocks are created when the incoming gas collides with the pressure barrier (*left-middle*). The gas bounces off and expands quasi-spherically and homologously at supersonic speeds (*right-middle* and *right*).

exchange between gas at different mass shells. Unlike other cases where the radiation energy is dominant, in this case, the gas internal energy is comparable to the radiation energy and the total internal energy drops like $\propto t^{-4/3}$, resulting in a non-power-law decay curve for $\overline{T}$. Although each of the two quantities, $\overline{\rho}$ and $\overline{T}$, tends to follow a single power law, the degree to which their magnitudes depend on $R_\star$, b, and $v_{\rm rel}$ is different. $\overline{\rho}$ has a very weak dependence on b and $R_\star$. $\overline{T}$ is insensitive to b and weakly depends on $R_\star$: only a factor of 1.5 greater for $R_\star = 100\,\mathrm{R}_\odot$ than that $R_\star = 10\,\mathrm{R}_\odot$.

$v^{\rm r}_{\rm peak}$ stays constant upon collision at (3–6) $\times$ $v_{\rm rel}$. The constant $v^{\rm r}_{\rm peak}$ phase lasts longer for the case involved with stronger shocks (e.g. larger $R_\star$ for given b and $v_{\rm rel}$). Eventually, $v^{\rm r}_{\rm peak}$ decreases over time because of the interactions with the background medium, following a power law of $t^{-1/3}$ for all models. In particular, the peak

Downloaded from https://academic.oup.com/mnras/article/528/4/6193/7603392 by Deutsches Elektronen Synchrotron DESY user on 18 December 2024

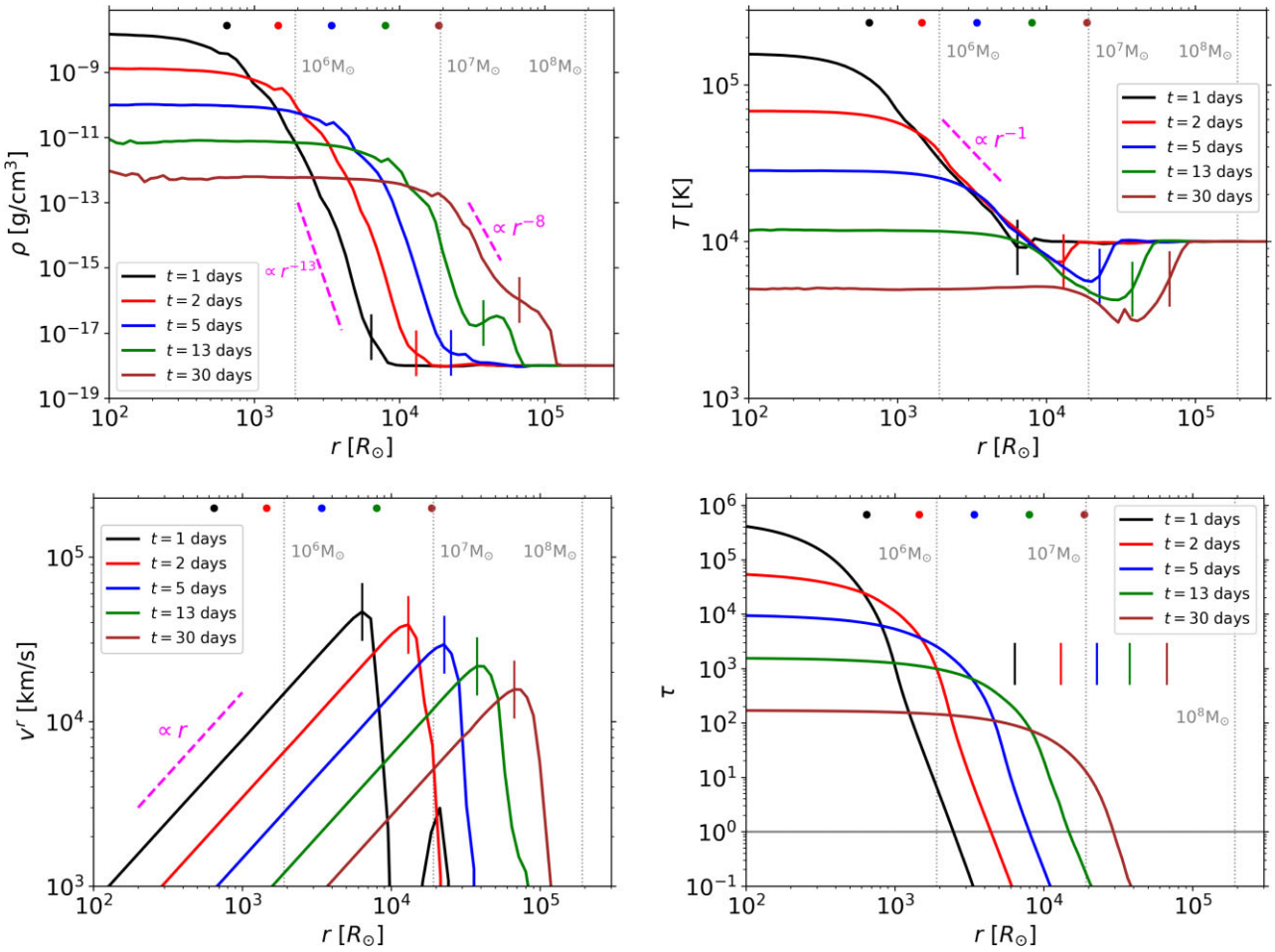

Figure 5. Spherically averaged density (*top-left*), temperature (*top-right*), radial velocity (*bottom-left*), and optical depth (*bottom-right*), of the expanding cloud produced in a collision between two 10 $R_\odot$ giants, as a function of radius from the collision point at five different times. The averages of the temperature and radial velocity are mass weighted. The optical depth is estimated by radially integrating $\kappa\rho dr$ inwards from 20× the distance of the core from the collision point. The three vertical lines show the distance from the BH with mass 10^6, 10^7, and 10^8 $M_\odot$ at which the Keplerian velocity is the same as the initial relative velocity. In other words, by the time the outer edge reaches the distances, the gas would meet the central BH. The dots indicate the locations of the cores at the five times, sharing the same colours with the lines. The vertical bars indicate the location of the outer edge where the expansion velocity is the maximum.

expansion speed with varying $R_\star$ tends to asymptote to a single value at later times. As b and $v_{\rm rel}$ decrease, $v^{\rm r}_{\rm peak}$ is smaller at a given time. But the difference is at most by a factor of 3 for the collision parameters considered.

As explained for our fiducial model above, the optical depth is initially high at collision, $\tau > O(10^6)$. The optical depth for most cases gradually decreases as the gas cloud expands, following a power law of $t^{-7/3}$, which is expected from the scaling relations of ρ and $v^{\rm r}_{\rm peak}$: $\tau \propto \rho R_{\rm peak} \propto t^{-3}t^{2/3} \propto t^{-7/3}$, where $R_{\rm peak}$ is the location of the peak expansion speed $\simeq v^{\rm r}_{\rm peak}t \propto t^{2/3}$. Note that we assume a constant opacity to find the scaling relation given that the electron scattering is the dominant source of opacities in the gas cloud. The deviation from the $t^{-7/3}$ power-law relation becomes more significant as the collisions happen at lower $v_{\rm rel}$ and higher b.

3.2.3 *Fitting formulae*

Combining all the scaling relations, we find that the average density $\overline{\rho}(t)$, mass-weighted average of temperature $\overline{T}$ peak expansion velocity $v^{\rm r}_{\rm peak}(t)$, size of the outer edge $R_{\rm peak}(t)$, and radial expansion speed $v^{\rm r}_{\rm peak}(r,t)$ after $t > 5$ d can be well described by the following analytical expressions:

$$\overline{\rho}(t) = 6\times10^{-10}\,{\rm g\,cm^{-3}}\left(\frac{t}{1\,{\rm d}}\right)^{-3}\left(\frac{v_{\rm rel}}{10^4\,{\rm km\,s^{-1}}}\right)^{-3}, \quad (2)$$

$$\overline{T}(t) = 1.5\times10^5\,{\rm K}\left(\frac{t}{1\,{\rm d}}\right)^{-1}\tan^{-1}(\sqrt{R_\star/10\,{\rm R_\odot}}) \quad \text{for } v_{\rm rel}\geq 5000\,{\rm km\,s^{-1}} \text{ and } b\lesssim 0.4\ R_\star, \quad (3)$$

$$\tau(t) = 2.5\times10^5\left(\frac{t}{1\,{\rm d}}\right)^{-7/3}, \quad \text{for } v_{\rm rel} > 5000\,{\rm km\,s^{-1}} \text{ and } b\lesssim 0.4\ R_\star, \quad (4)$$

$$v^{\rm r}_{\rm peak}(t) = 50\,000\,{\rm km\,s^{-1}}\left(\frac{t}{1\,{\rm d}}\right)^{-1/3}\left(\frac{v_{\rm rel}}{10^4\,{\rm km\,s^{-1}}}\right)^{0.7}\times\left(\frac{b/R_\star+5}{5}\right)^{-4}, \quad (5)$$

Downloaded from https://academic.oup.com/mnras/article/528/4/6193/7603392 by Deutsches Elektronen Synchrotron DESY user on 18 December 2024

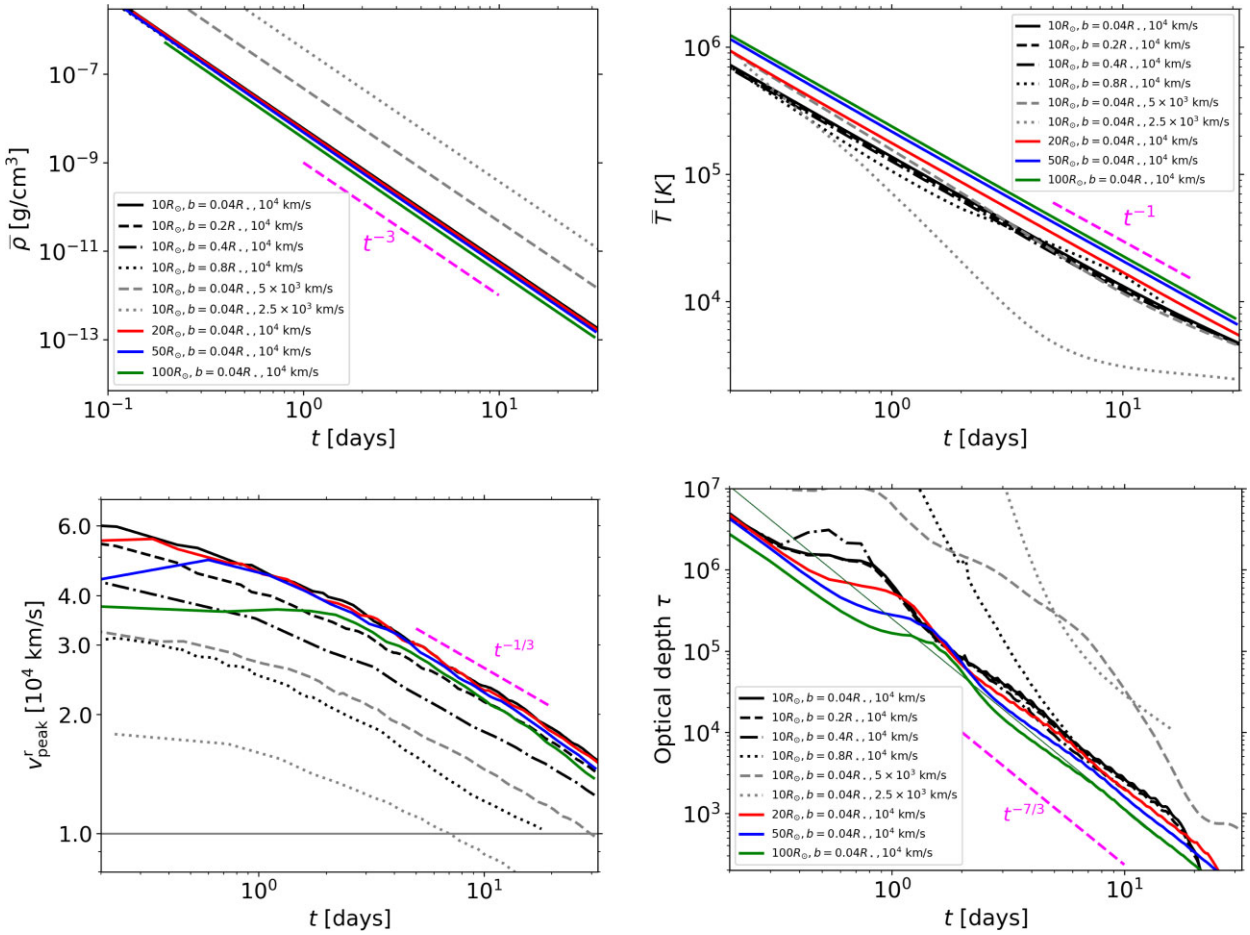

Figure 6. Average density $\overline{\rho}$ (*top-left*), mass-weighted average of temperature $\overline{T}$ (*top-right*), the peak expansion speed $v^{\rm r}_{\rm peak}$ (*bottom-left*), and the surface average of the optical depth τ to the centre (*bottom-right*) of the cloud in all models, as a function of time since collision. The average density and temperature are estimated using the cells within a radius containing 75 per cent of the cloud mass.

$$R_{\rm peak}(t) = 6.5 \times 10^{14} \left(\frac{t}{1\,{\rm d}}\right)^{2/3} \left(\frac{v_{\rm rel}}{10^4\,{\rm km\,s^{-1}}}\right)^{0.7} \times \left(\frac{b/R_\star + 5}{5}\right)^{-4}, \quad (6)$$

$$v^{\rm r}(r,t) = \begin{cases} v^{\rm r}_{\rm peak}\left(\frac{r}{R_{\rm peak}}\right) & \text{for } r \le R_{\rm peak}, \\ 0 & \text{for } r > R_{\rm peak}, \end{cases} \quad (7)$$

where the expression for $R_{\rm peak}$ is found by analytically integrating $v^{\rm r}(r,\,t)$ over time. Note that $\overline{\rho}$ decays faster than that expected from the expression $3M_{\rm gas}/(4\pi R^3_{\rm peak}) \simeq t^{-2}$ because $\overline{\rho}$ follows the homologous relation whereas the peak expansion speed slows down so the outer edge expands slower than that expected for homologous expansion.

Note that we do not include the term describing the dependence on $R_\star$ in most of the expressions above because of their very weak $R_\star$ dependence. On the other hand, the omission of the $v_{\rm rel}$ dependence in equation (3) for $\overline{T}$ is because of too small number of models with varying $v_{\rm rel}$ for reliable fitting. Instead, we have specified the range of $v_{\rm rel}$ where the equation is valid.

3.3 Stellar core

The cores move almost synchronously with the bulk of the gas. The orbit of the cores are barely affected by the collision: they remain unbound after collision and move away from each other at a speed almost same as the incoming speed. The distances from the collision point in our fiducial model at five different times are marked with circles in Fig. 5.

The mass bound to the cores is larger for larger $v_{\rm rel}$ and smaller b. But it is overall insignificant. For $b \le 0.2\,{\rm R}_\odot$ and $v_{\rm rel} \ge 5000$ km s^{-1}, the bound mass is less than $6 \times 10^{-6}\,{\rm M}_\odot$. It is $\simeq 2 \times 10^{-3}\,{\rm M}_\odot$ for the model with $v_{\rm rel} = 2500$ km s^{-1} and that with $b = 0.4\,{\rm R}_\odot$ and $\simeq 3 \times 10^{-2}\,{\rm M}_\odot$ for the model with $b = 0.8\,{\rm R}_\odot$.

3.4 Conversion factor

In this section, we investigate how much heat energy is created in collisions, which is closely related to the amount of energy that can be radiated away and potentially observed. We first define the conversion factor $\eta_{\rm rad}$ as the ratio of the total radiation energy to the initial kinetic energy,

$$\eta_{\rm rad}(t) = \frac{\int aT(t)^4 {\rm d}V}{\int 0.5\rho(t=0)v(t=0)^2 {\rm d}V}, \quad (8)$$

Downloaded from https://academic.oup.com/mnras/article/528/4/6193/7603392 by Deutsches Elektronen Synchrotron DESY user on 18 December 2024

Table 2. Peak conversion factor η, luminosity at peak $L_{\rm peak}$ and blackbody temperature at peak $T_{\rm BB,peak}$ for each model, using equation (11) ($L_{\rm peak,1}$ and $T_{\rm BB,peak,1}$) and equation (12) ($L_{\rm peak,2}$ and $T_{\rm BB,peak,2}$).

Model number	$R_\star$ $\rm R_\odot$	$v_{\rm rel}$ $\times 10^3$ km s^{-1}	b $R_\star$	$\eta_{\rm peak}$	$L_{\rm peak,1}$ $\times 10^{43}$ erg s^{-1}	$L_{\rm peak,2}$ $\times 10^{43}$ erg s^{-1}	$T_{\rm BB,peak,1}$ $\times 10^5$ K	$T_{\rm BB,peak,2}$ $\times 10^5$ K
1	10	10	0.04	0.69	9.6	1.3	3.0	2.1
2	10	10	0.2	0.59	9.3	1.3	2.9	2.0
3	10	10	0.4	0.41	6.5	1.0	2.7	1.9
4	10	10	0.8	0.13	4.2	0.7	2.7	1.7
5	10	5	0.04	0.69	2.1	0.3	2.2	1.4
6	10	2.5	0.04	0.56	0.5	0.1	1.0	1.0
7	20	10	0.04	0.65	13	2.0	2.7	1.7
8	50	10	0.04	0.73	26	3.4	2.2	1.4
9	100	10	0.04	0.73	26	3.4	1.7	1.1

where a is the radiation constant and dV is the volume element of each cell. Using $\eta_{\rm rad}$, one can estimate the total radiation energy as $\simeq 0.25\eta_{\rm rad}\, M_\star v_{\rm rel}^2$ for equal-mass collisions. To distinguish gas that initially belonged to the stars from the background gas, we employ a selection condition using a passive scalar. The passive scalar is an artificial scalar quantity initially assigned to each cell which then evolves via advection without affecting the evolution of hydrodynamics quantities. The initial values of the passive scalar of the cells in the stars are 1 and that of the background cells is 0. So depending on the mass exchange (or mixing) between the cells, the passive scalar varies between 0 (vacuum cells) and 1 (cells originally in the stars). We perform the integration over cells with the passive scalar $\gtrsim$0.1. The value of $\eta_{\rm rad}$ is largely unaffected by the choice of the threshold of the passive scalar, provided that it is greater than 0.

We show $\eta_{\rm rad}$ for all our models in Fig. 8 before the radiation energy in the optically thin gas becomes dominant. It is generally found that $\eta_{\rm rad}$ dramatically increases at collision to $\eta_{\rm rad} \simeq 0.1$–$0.8$, meaning a significant fraction of the initial kinetic energy is converted into heat energy. The maximum conversion factors are summarized in Table 2. Then, as the cloud expands and cools, $\eta_{\rm rad}$ decreases down to $\lesssim 10^{-2}$. We see three clear post-peak trends of $\eta_{\rm rad}$. First, $\eta_{\rm rad}$ is larger when larger stars collide. Additionally, $\eta_{\rm rad}$ is approximately $\propto R_\star$ at any given time: $\simeq$(1–2) $\times\, 10^{-3}$ for $R_\star = 10\,\rm R_\odot$, $\simeq$(3–4) $\times\, 10^{-3}$ for $R_\star = 20\,\rm R_\odot$, $\simeq 10^{-2}$ for $R_\star = 50\,\rm R_\odot$, and $\simeq 2 \times 10^{-2}$ for $R_\star = 100\,\rm R_\odot$ at $t \simeq 3$ d. We attribute this positive correlation between $\eta_{\rm rad}$ and $R_\star$ to the fact that for the same relative velocity, larger (cooler) stars collide at higher $\mathcal{M}$, resulting in stronger shocks over a wider contact surface ($\propto R_\star$). Secondly, $\eta_{\rm rad}$ is almost the same when $b \lesssim 0.2\,R_\star$, while $\eta_{\rm rad}$ begins to decrease with b when $b \gtrsim 0.2\,R_\star$. This trend is somewhat expected given that as b increases, the mass of gas that is shocked at collision decreases. Lastly, $\eta_{\rm rad}$ decreases with $v_{\rm rel}$ because of lower $\mathcal{M}$ collisions for given sound speed (i.e. the same star). $\eta_{\rm rad}$ at $v_{\rm rel} = 5000$ km s^{-1} is almost the same as that at $v_{\rm rel} = 10\,000$ km s^{-1}, but $\eta_{\rm rad}$ at $v_{\rm rel} = 2500$ km s^{-1} is lower by a factor of $\simeq$2 than that for our fiducial case. The overall levels of the conversion factors that we obtain are comparable to what Amaro Seoane (2023b) imposed in order for their analytical model to match with the observed object ZTF19acboexm (see their fig. 9).

We can also define the conversion factor for the ram pressure of gas moving at supersonic speeds,

$$\eta_{\rm ram}(t) = \frac{\int \rho(t) v(t)^2 {\rm d}V}{\int \rho(t=0) v(t=0)^2 {\rm d}V}, \tag{9}$$

where the integration in the denominator is carried out over cells for which the passive scalar >0.1, and that in the numerator the integration is carried out only over cells with supersonic speeds, $\mathcal{M} \geq 1$. As illustrated in the third column panels of Figs 4 and 7, almost all the gas is supersonically expanding. As a result, $1 - \eta_{\rm ram} \simeq \eta_{\rm rad}$.

3.5 Observables

We estimate the luminosity L, blackbody radius $R_{\rm BB}$, and temperature $T_{\rm BB}$, using the radiation energy and the local cooling time $t_{\rm cool}$. We first construct a spherical grid with an extremely small opening polar angle ($\theta \simeq 10^{-10}$ rad) to avoid the singularity at the poles, radially extending out to near the outer boundary of the domain. The grid in the radial direction is logarithmically divided, i.e. constant $\Delta r/r$ where Δr is the cell size at r, while that in the θ and ϕ directions are linearly divided, i.e. constant $\Delta\theta$ and $\Delta\phi$. The number of grids in r, θ, and ϕ are (800, 600, 600), which we confirmed to give converging estimates for the observables. We then identify the photosphere at which the optical depth $\tau \simeq 1$. τ is integrated along each r-path with the opacity found using an OPAL opacity table for Solar metallicity (Iglesias & Rogers 1996). The photospheric area is

$$A_{\rm BB} = \int_0^{2\pi} \int_{\simeq 0}^{\simeq \pi} r(\tau = 1)^2 \sin\theta {\rm d}r {\rm d}\theta {\rm d}\phi, \tag{10}$$

which gives the effective size of the emitting region or blackbody radius $R_{\rm BB} = (A_{\rm BB}/4\pi)^{1/2}$.

We attempt to bracket the range of realistic radiated luminosity from the collision event by employing two different methods, each of which places different weights on the contribution from the gas cloud layers (the inner regions or outer regions near the photosphere) within the identified photosphere. Our estimates should be accurate at an order-of-magnitude level. However, for more accurate modelling of light curves, we will carry out detailed non-equilibrium radiation transport calculations in future follow-up work dedicated to estimating light curves and spectra.

In both methods, the total luminosity for each radial path is estimated by summing the contributions from the cells with the local cooling time $t_{\rm cool}$ shorter than the evolution time t within the photosphere. Here, $t_{\rm cool}$ is defined as $h_\rho \tau (1 + u_{\rm gas}/u_{\rm rad})/c$ where h_ρ is the density moment scale height inside the photosphere and $u_{\rm rad}$ ($u_{\rm gas}$) is the radiation (gas thermal) energy. However, the difference between the two methods is the assumption for how most of the radiation energy is radiated away. In one method, we assume that the total radiation energy within the photosphere is radiated away over a time comparable to the cooling time at the base of the cloud. Under this assumption, the inner regions tend to dominate the luminosity. We first integrate the total radiation energy along the radial path and divide it by the cooling time at the base of the cloud $t_{\rm cool,max}$, i.e. the

Downloaded from https://academic.oup.com/mnras/article/528/4/6193/7603392 by Deutsches Elektronen Synchrotron DESY user on 18 December 2024

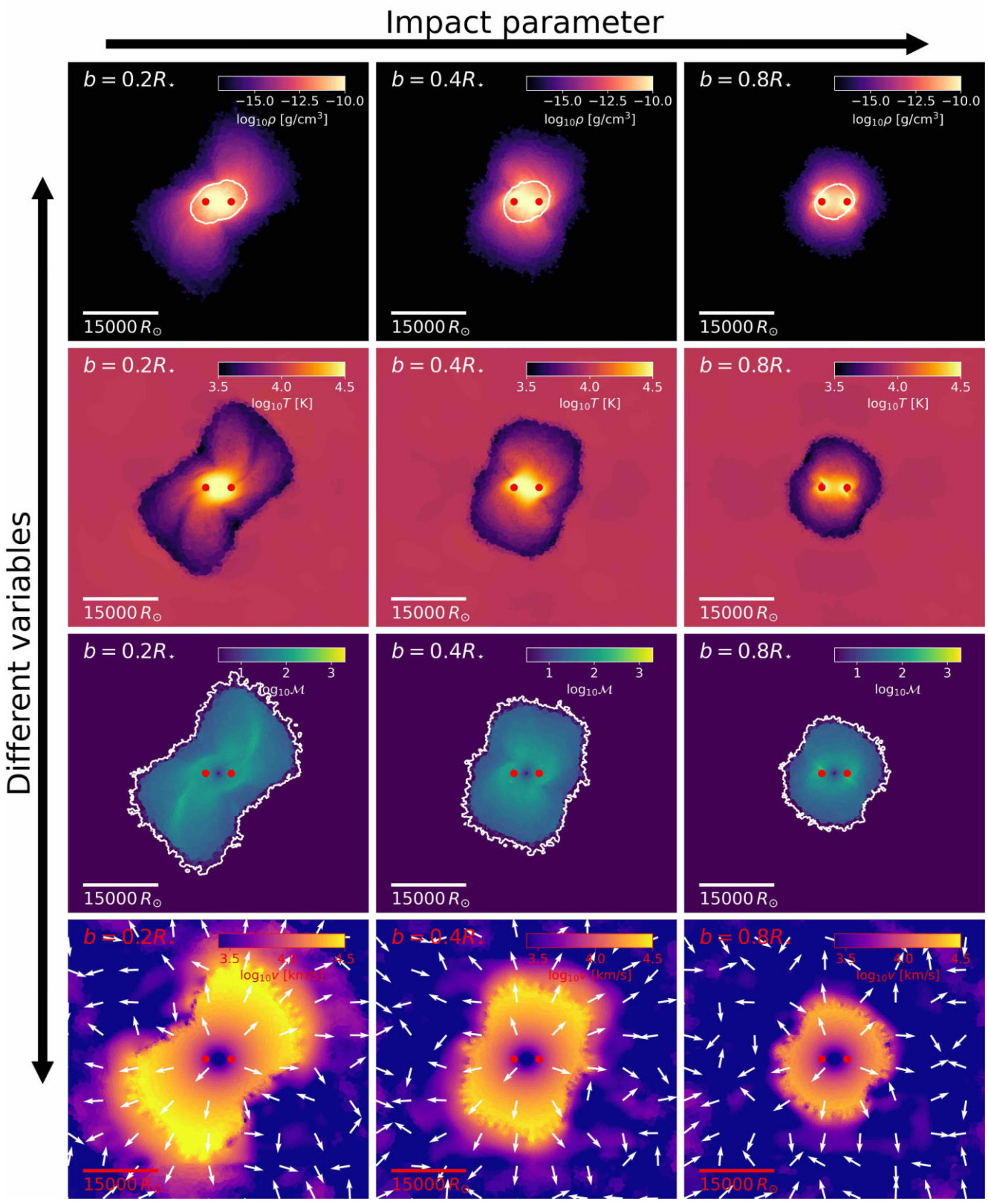

Figure 7. Same as Fig. 4, but for off-axis collisions ($b = 0.2$, 0.4, and $0.8\,R_\star$) between two giants with $R_\star = 10\,\mathrm{R}_\odot$ at $t \simeq 5$ d since collision.

Downloaded from https://academic.oup.com/mnras/article/528/4/6193/7603392 by Deutsches Elektronen Synchrotron DESY user on 18 December 2024

longest cooling time which is no longer than t, or

$$L_1 = \int_0^{2\pi} \int_{\simeq 0}^{\simeq \pi} \left[\int_{r(t_{\rm cool}=t)}^{r(\tau=1)} aT^4 r^2 \sin\theta {\rm d}r \right] t_{\rm cool,max}(\theta,\phi)^{-1} {\rm d}\theta {\rm d}\phi. \quad (11)$$

In the second, we assume that the radiation energy of each cell is radiated away over the local cooling time. So the total luminosity is estimated,

$$L_2 = \int_0^{2\pi} \int_{\simeq 0}^{\simeq \pi} \int_{r(t_{\rm cool}=t)}^{r(\tau=1)} aT^4 t_{\rm cool}(r,\theta,\phi)^{-1} r^2 \sin\theta {\rm d}r {\rm d}\theta {\rm d}\phi. \quad (12)$$

In this method, the outer regions near the photosphere dominate the luminosity. As stressed before, the evolution of the hydrodynamics quantities for optically thin gas (i.e. outer region near the photosphere) in our simulations is intrinsically less accurate than those for optically thick gas. Hence, L_1 should be considered more consistent with our hydrodynamical scheme. We find that the shapes of the L_1 and L_2 light curves are very similar. However, L_1 is consistently smaller than L_2 by a factor of $\simeq$10. For this reason, we present L_1 and the resulting blackbody temperature $T_{\rm BB,1} = (L_1/\sigma A_{\rm BB})^{1/4}$ in this section and those from equation (12) in Appendix A.

Fig. 9 shows L_1 (*top*), $T_{\rm BB,1}$ (*middle*), and $R_{\rm BB}$ (*bottom*) as a function of time measured since collision for all our models.[5] Note that the luminosity and the blackbody temperature differ depending on the assumption of radiation (equations 11 and 12), but $R_{\rm BB}$ is independent of the assumption. The luminosity increases dramatically to its peak at collision. The peak luminosity is $L_1 \gtrsim 10^{41}$–10^{43} erg s^{-1} ($L_2 \gtrsim 10^{42}$–10^{44}), which is higher for larger $R_\star$ and smaller b and higher $v_{\rm rel}$, which has the same trend as $\eta_{\rm rad}$. The temperature at peak is $T_{\rm BB,1} \simeq 10^5$ K. Because $T_{\rm BB} \propto L^{1/4}$, $T_{\rm BB,2}$ is greater than $T_{\rm BB,1}$ by less than a factor of 2. We summarize peak L and $T_{\rm BB}$ at peak for all our models in Table 2. Subsequently both L and $T_{\rm BB}$, independent of the assumption for the diffusion time (so both L_1 and L_2), decrease following a power law of $\propto t^{-\xi}$ with ξ slightly differing at early and late times. L at $t \lesssim 5$ d reveals a decaying curve with $\xi \simeq 0.7$–0.8, followed by a slower decay with $\xi \simeq 0.4$ at $t \gtrsim 5$ d. L therefore decreases by a factor of 10 for the first 5 d. The decay in L for the next 30 d is relatively small, by only by a factor of a few. The change in ξ for $T_{\rm BB}$ is very mild: $\xi \simeq 0.6$ at $t \lesssim 5$ d and $\simeq 0.5$ at $t \gtrsim 5$ d. $T_{\rm BB}$ decreases from $\simeq$(1–2) $\times$ 10^5 K at collision to 10^4 K at 5–15 d, (4–6) $\times$ 10^3 K at 30 d. This means the collision will be bright in extreme ultraviolet (UV) at collision which shifts to optical on a time-scale of a month. Lastly, $R_{\rm BB}$ increases to $\simeq 10^{15}$cm in 30 d, approximately following power-law growth of $\propto t^{0.8}$.

The light curves from our simulations reveal some differences from that analytically predicted by Amaro Seoane (2023b). Assuming a constant η comparable to the minimum $\eta_{\rm rad}$ shown in Fig. 8, their analytical model predicts a peak luminosity consistent with the numerically integrated peak luminosity shown in Fig. 9. However, the luminosity from their analytical model peaks at a few days after collision and subsequently decays faster. We attribute these discrepancies to the difference in the way of calculating the luminosity. In their analytical model, the luminosity was estimated under the assumption that η does not change over time and the total radiation energy within the gas cloud is radiated away instantaneously on a time-scale comparable to the longest possible photon cooling time at any given time (e.g. based on the optical depth to the centre). On the other hand, in this work, we take into account the time-dependent contributions (e.g. adiabatic loss of energy due to expansion) of the cloud.

[5]While this paper is under review, we published Dessart et al. (2024) in which we conducted detailed radiation transfer calculations for the observables of BDCs using the time-dependent radiation transfer code CMFGEN (Hillier & Dessart 2012). The more accurately estimated luminosity and temperature are in good agreement with our order-of-magnitude estimates assuming the inner regions dominating the luminosity (equation 11) shown in Fig. 9.

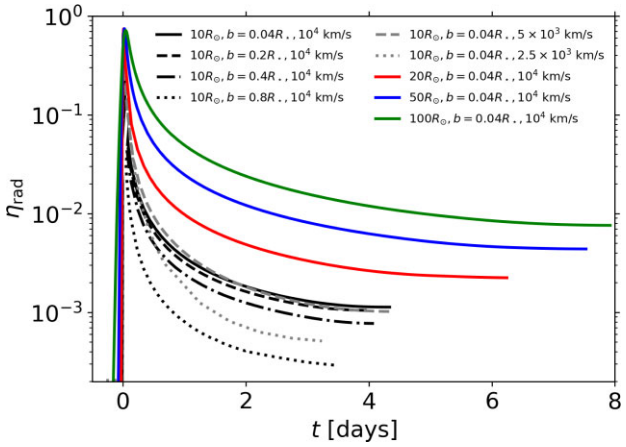

Figure 8. The ratio of the radiation energy to the initial kinetic energy $\eta_{\rm rad}$ as a function of time, measured since collision, for all our models.

The observables estimated in this section are driven by stellar collisions. But given the fact that these collisions occur near an SMBH, the expanding gas cloud and the nearby BH would very likely interact, generating a possibly even brighter flare, which we discuss in Section 4.2.

4 DISCUSSION

4.1 Interaction of gas cloud with interstellar medium

In this work, we simulated high-velocity collisions of giants surrounded by a medium with a constant density of 10^{-18}g cm^{-3} and temperature of 10^4 K. As the cloud expands, it collides inelastically with the background medium, which results in the continuous decrease in the kinetic energy of the expansion front. In addition, the collision between the outer edge of the cloud and the background medium can create shocks, converting the kinetic energy into heat energy. The net effect is the deceleration of the gas cloud, deviating from a homologous behaviour, which is also found from our simulations where the velocity of the outer edge decreases following $t^{-1/3}$. This impact of the surrounding medium would be faster if the colliding stars were initially embedded in a denser medium. For example, the rising slope of $\eta_{\rm rad}$ would be less steep for the case with lower density background gas. Given the supersonic motion of the cloud, how the cloud expands would not be significantly affected by the temperature of the background medium for a given background density. However, the evolution of $\eta_{\rm rad}$ would be changed depending on the background temperature. In fact, we performed extra simulations with different background temperatures (100–5000 K), showing that while the expansion properties of the cloud (e.g. $\overline{\rho}$, $\overline{T}$, and $v^{\rm r}_{\rm peak}$) are almost independent of the background temperature, $\eta_{\rm rad}$ tends to be lower at the local minimum and increases more slowly afterward for a lower background temperature.

Although the deviation from a homologous expansion was only found near the outer edge for the duration of our simulations, as an order-of-magnitude estimate, the motion of the entire gas cloud would become completely deviated from a homologous expansion

Downloaded from https://academic.oup.com/mnras/article/528/4/6193/7603392 by Deutsches Elektronen Synchrotron DESY user on 18 December 2024

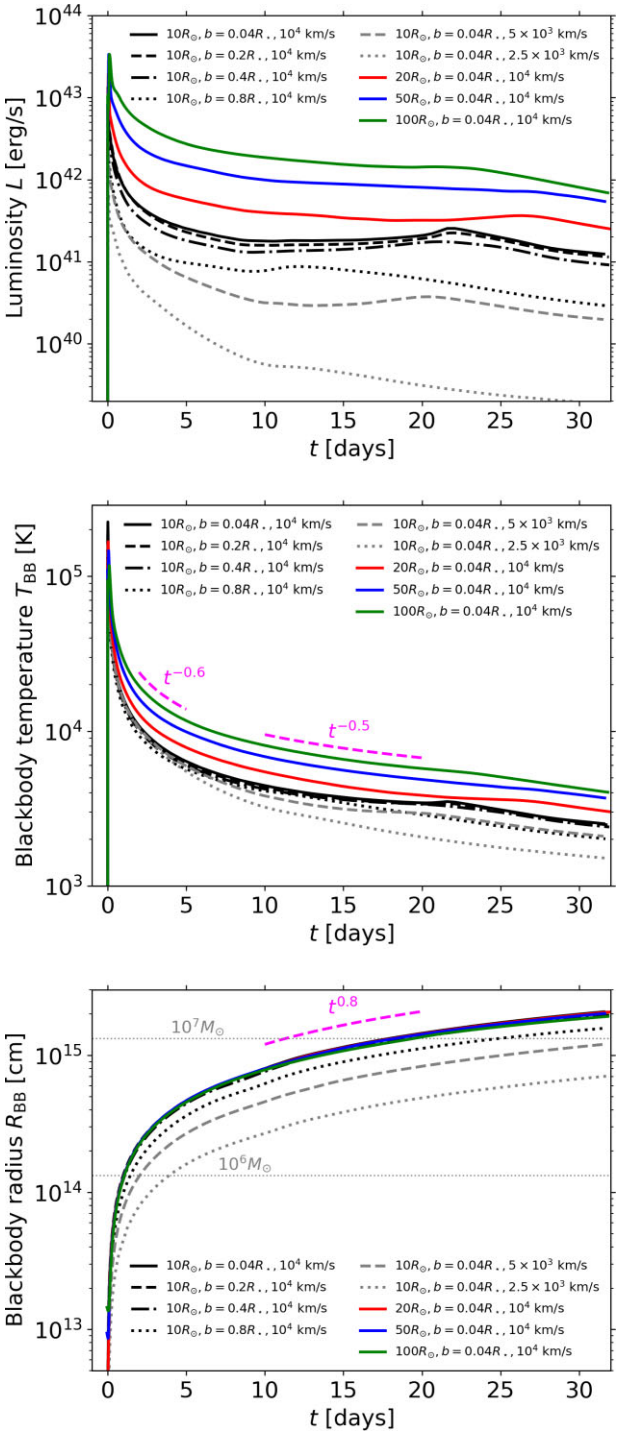

Figure 9. Bolometric luminosity L (*top*), blackbody temperature $T_{\rm BB}$ (*middle*), and blackbody radius $R_{\rm BB}$ (*bottom*), estimated for stellar collisions using equations (10) and (11). The dotted grey horizontal lines in the *bottom* panel indicate the distances of the collision from the black hole with $M_{\rm BH} = 10^6\,{\rm M}_\odot$ ($\simeq 10^{14}$ cm) and $10^7\,{\rm M}_\odot$ ($\simeq 10^{15}$ cm). The magenta guide lines show the power law that describes the quantity shown in the last two panels.

when the swept-up mass is comparable to the mass of the cloud,

$$t_{\rm non\text{-}homologous} \simeq \frac{3M_{\rm gas}}{4\pi\rho_{\rm ISM}(v^{\rm r})^3}, \simeq 1100\,{\rm d}\left(\frac{M_{\rm gas}}{2\,{\rm M}_\odot}\right)\left(\frac{\rho_{\rm ISM}}{10^{-18}\,{\rm g\,cm^{-3}}}\right)^{-1}\left(\frac{v^{\rm r}}{10^4\,{\rm km\,s^{-1}}}\right), \quad (13)$$

where $v^{\rm r}$ is the expansion speed and $\rho_{\rm ISM}$ the density of the background medium. At the same time, this also means that the scaling relations for the homologous expansion found from our simulations would be applied to the evolution of the homologously expanding part of the collision product, independent of the existence of the background medium.

4.2 Interaction of gas cloud with supermassive black hole

In addition to the burst caused by the stellar collision (see Section 3.5), there would be a subsequent burst due to accretion on to the nearby SMBH. As a result, the overall shape of the luminosity would be that the stellar collision creates the first peak with $L \gtrsim 10^{42}$ erg s^{-1} which decays, followed by a sharp rise to Eddington due to accretion on to the BH, possibly remaining at that level for up to years until the captured gas is accreted on to the BH. We will examine the observables from the BH–cloud interaction by considering two cases: (1) Case 1: no-decelerating expansion (Section 4.2.1) and (2) Case 2: decelerating expansion (Section 4.2.2). For simplicity, we assume that the centre-of-mass motion of the collision product is moving sufficiently slowly compared to the cloud expansion speed, which would be relevant for head-on equal-mass collisions. In addition, we make a crude assumption that the gas cloud is expanding spherically. However, in reality, the collision product can have a non-negligible coherent motion compared to the SMBH and the shape of the gas cloud would be deformed by the tidal force of the SMBH. These will be studied in detail in a follow-up project. And we will discuss the astrophysical implications for BHs in Section 4.2.3.

4.2.1 Case 1: no-decelerating expansion

We first assume that the entire gas cloud expands homologously and the expansion speed of the outer edge is $v^{\rm r} \simeq \psi v_{\rm rel}$ with $\psi \simeq 3$–6 (see Fig. 6). The gas cloud starts to interact with the BH when the size of the expanding gas cloud becomes comparable to the distance to the BH $R_{\rm BB}$ for given $v_{\rm rel}$,

$$R_{\rm BH} \simeq \frac{GM_\bullet}{v_{\rm rel}^2} = 10^{15}\,{\rm cm}\left(\frac{M_\bullet}{10^7\,{\rm M}_\odot}\right)\left(\frac{v_{\rm rel}}{10^4\,{\rm km\,s^{-1}}}\right)^{-2}. \quad (14)$$

The time difference between the first collision-driven burst and the subsequent accretion-driven burst would be set by the time $\tau_{\rm BH}$ at which the outer edge of the cloud reaches the BH, $R_{\rm BH} - R_{\rm Sch} \simeq R_{\rm BH} \simeq R_{\rm peak}$, where $R_{\rm Sch}$ is the Schwarzschild radius,

$$\tau_{\rm BH} \simeq \frac{R_{\rm BH}}{v^{\rm r}} \simeq 3\,{\rm d}\left(\frac{M_\bullet}{10^7\,{\rm M}_\odot}\right)\left(\frac{v_{\rm rel}}{10^4\,{\rm km\,s^{-1}}}\right)^{-3}. \quad (15)$$

To zeroth order, the part of the cloud that is within the Bondi radius $R_{\rm Bondi} \simeq 2GM_\bullet/(v^{\rm r})^2$ from the BH would be gravitationally captured by the BH and subsequently accreted on to the BH. Assuming a Bondi–Hoyle accretion (Bondi & Hoyle 1944; Bondi 1952), the

Downloaded from https://academic.oup.com/mnras/article/528/4/6193/7603392 by Deutsches Elektronen Synchrotron DESY user on 18 December 2024

luminosity $L_{\rm Bondi}$ with radiative efficiency ϵ can be estimated,

$$L_{\rm Bondi} \simeq \frac{4\pi\epsilon G^2 M_\bullet^2 \rho c^2}{(v^{\rm r})^3}, \simeq 3\times10^{47}\ {\rm erg\,s^{-1}} \left(\frac{\epsilon}{0.1}\right)\left(\frac{M_\bullet}{10^7\ {\rm M_\odot}}\right)^{-1}\left(\frac{v_{\rm rel}}{10^4\ {\rm km\,s^{-1}}}\right)^3, \quad (16)$$

which is super-Eddington for $M_\bullet < 3\times10^8\,{\rm M_\odot}(v_{\rm rel}/10^4\,{\rm km\,s^{-1}})^{1.5}$. Note that $L_{\rm Bondi}$ has no dependence on t given the scaling relations for ρ ($\propto t^{-3}$, equation 2) and $v^{\rm r}(r = R_{\rm BH})$ ($\propto t^{-1}$, equation 7): $L_{\rm Bondi} \propto \rho(v^{\rm r})^{-3} \propto t^0$. Super-Eddington accretion may be possible if the gas is optically thick and the trapping radius $R_{\rm tr} = (L_{\rm Bondi}/L_{\rm Edd})(GM_\bullet/\epsilon c^2)$ is smaller than the Bondi radius (Begelman 1979). The ratio of the two radii is

$$\frac{R_{\rm tr}}{R_{\rm Bondi}} \simeq 300\left(\frac{t}{1\,{\rm d}}\right)^{-2}\left(\frac{v_{\rm rel}}{10^4\,{\rm km\,s^{-1}}}\right)^{-1}, \quad (17)$$

suggesting super-Eddington accretion would be possible at $t \gtrsim 20\ {\rm d}(v_{\rm rel}/10^4\,{\rm kms^{-1}})^{-0.5}$. Here, we caution that the time ratio in equation (17) is estimated under the assumption that the global accretion flow is not affected by any accretion feedback, which is highly uncertain. Assuming a blackbody, the temperature at the Bondi radius if $L \simeq L_{\rm Edd}$ is

$$T_{\rm Bondi}(t) \simeq 10^5\,{\rm K}\left(\frac{t}{3\,{\rm d}}\right)^{-1}\left(\frac{M_\bullet}{10^7\ {\rm M_\odot}}\right)^{3/4}\left(\frac{v_{\rm rel}}{10^4\,{\rm km\,s^{-1}}}\right)^{-1/2}, \quad (18)$$

and at the onset of the BH–gas interaction (or $t \simeq \tau_{\rm BH}$),

$$T_{\rm Bondi}(t=\tau_{\rm BH}) \simeq 10^5\,{\rm K}\left(\frac{\psi}{5}\right)\left(\frac{M_\bullet}{10^7\ {\rm M_\odot}}\right)^{-1/4}\left(\frac{v_{\rm rel}}{10^4\,{\rm km\,s^{-1}}}\right). \quad (19)$$

If $L \simeq L_{\rm Bondi}$,

$$T_{\rm Bondi} \simeq 2.4\times10^4\,{\rm K}\left(\frac{t}{150\,{\rm d}}\right)^{-1}\left(\frac{\epsilon}{0.1}\right)^{1/4} \times\left(\frac{M_\bullet}{5\times10^8\ {\rm M_\odot}}\right)^{1/4}\left(\frac{v_{\rm rel}}{10^4\,{\rm km\,s^{-1}}}\right)^{-5/4}, \quad (20)$$

and at $t = \tau_{\rm BH}$,

$$T_{\rm Bondi}(t=\tau_{\rm BH}) \simeq 2.4\times10^4\,{\rm K}\left(\frac{\psi}{5}\right)\left(\frac{\epsilon}{0.1}\right)^{1/4} \times\left(\frac{M_\bullet}{5\times10^8\ {\rm M_\odot}}\right)^{-3/4}\left(\frac{v_{\rm rel}}{10^4\,{\rm km\,s^{-1}}}\right)^{-7/4}. \quad (21)$$

Because $R_{\rm Bondi}$ increases faster than $R_{\rm peak}$,

$$\frac{R_{\rm Bondi}}{R_{\rm peak}} \propto t, \quad (22)$$

as the most optimistic case, the entire gas cloud could be ultimately captured by the BH in a time $\tau_{\rm capture}$ at which $R_{\rm Bondi} \simeq R_{\rm peak}$,

$$\tau_{\rm capture} \simeq 40\ {\rm d}\left(\frac{\psi}{5}\right)\left(\frac{M_\bullet}{10^7\ {\rm M_\odot}}\right)\left(\frac{v_{\rm rel}}{10^4\,{\rm km\,s^{-1}}}\right)^{-3}. \quad (23)$$

Then, the maximum duration of the Eddington luminosity may be set by

$$\tau_{\rm acc} \lesssim \frac{M_{\rm gas}\epsilon c^2}{L_{\rm Edd}} \simeq 9\ {\rm yr}\left(\frac{\epsilon}{0.1}\right)\left(\frac{M_{\rm gas}}{2\ {\rm M_\odot}}\right)\left(\frac{M_\bullet}{10^7\ {\rm M_\odot}}\right)^{-1}, \quad (24)$$

where $M_{\rm gas}$ is the mass of the gas cloud, i.e. total mass of the two collided stars. Here, we assumed that the entire gas would be accreted on to the BH. However, radiation pressure from super-Eddington accretion would be strong enough to generate outflow. For such a case, only a fraction of the gas cloud would end up accreting and $\tau_{\rm acc}$ would be shorter than estimated above.

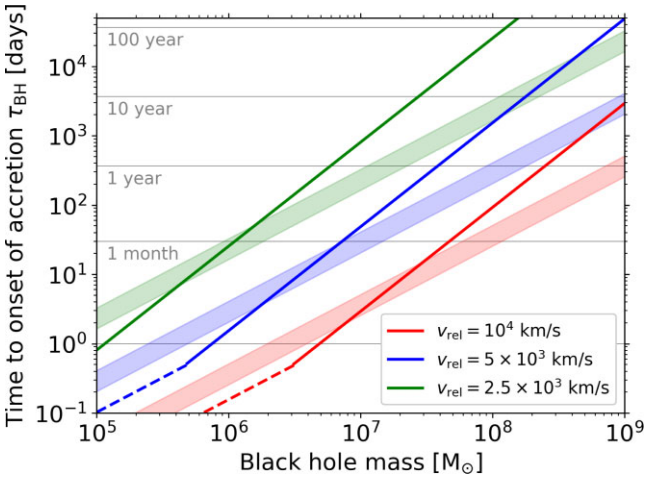

Figure 10. Time $\tau_{\rm BH}$ to the accretion-driven burst since the peak collision-driven luminosity for different collision velocities $v_{\rm rel}$, as a function of black hole mass. The lines illustrate *Case 2: decelerating expansion* (Section 4.2.2) where the entire cloud expands homologously up to 0.5 d since collision (dashed), then the outer edge starts decays like $t^{-1/3}$ (solid) due to interactions with a background medium, using equation (7). The less steep diagonal bars demarcate the range of $\tau_{\rm BH}$ for the case where the gas cloud continuously expands homologously with the outer edge moving at (3–6) $\times$ $v_{\rm rel}$ (*Case 1: no-decelerating expansion* (Section 4.2.1), corresponding to the peak expansion speed upon collision in our simulations (see the *bottom-right* panel of Fig. 6).

4.2.2 *Case 2: decelerating expansion*

Now we examine the observables from interactions between decelerating expanding cloud with $v^{\rm r}_{\rm peak} \propto t^{-1/3}$ and the SMBH, using equations (2)–(7). For this case, $\tau_{\rm BH}$ has a different dependence on $M_\bullet$ and $v_{\rm rel}$,

$$\tau_{\rm BH} \simeq 3\ {\rm d}\left(\frac{M_\bullet}{10^7\ {\rm M_\odot}}\right)^{3/2}\left(\frac{v_{\rm rel}}{10^4\,{\rm km\,s^{-1}}}\right)^{-3}\left(\frac{b/R_\star+5}{5}\right)^6, \quad (25)$$

We show in Fig. 10 the range of $\tau_{\rm BH}$ for three different collision velocities $v_{\rm rel}$ as a function of $M_\bullet$ assuming a non-decelerating expansion speed (thick diagonal bars, ψ = 3–6) and a decelerating expansion speed (solid lines). The interaction onset time would be longer generally if the expansion of the cloud slows down. Depending on $M_{\rm BH}$ and $v_{\rm rel}$, the second burst could happen over a wide range of time. For example, if a collision with $v_{\rm rel} \gtrsim 2500\,{\rm km\,s^{-1}}$ occurs in the Galactic centre (with $M_\bullet \simeq 4\times10^6\,{\rm M_\odot}$; GRAVITY Collaboration 2019), the second accretion-driven burst would occur after the collision in less than a day to 6–7 months depending on the location of the collision from the BH. For very massive black holes ($M_{\rm BH} > 10^8\,{\rm M_\odot}$), $\tau_{\rm BH}$ can be more than tens of years.

The Bondi luminosity is still independent of t and has the same $M_\bullet$ – and $v_{\rm rel}$ – dependence as the case with the no-decelerating expansion, but it is roughly a factor of 3 greater at given $M_{\rm BH}$ and $v_{\rm rel}$,

$$L_{\rm Bondi} \simeq 10^{48}\ {\rm erg\,s^{-1}}\left(\frac{\epsilon}{0.1}\right)\left(\frac{M_\bullet}{10^7\ {\rm M_\odot}}\right)^{-1}\left(\frac{v_{\rm rel}}{10^4\,{\rm km\,s^{-1}}}\right)^3, \quad (26)$$

which is further illustrated in Fig. 11. While the expression for the blackbody temperature at the Bondi radius has the same dependence

Downloaded from https://academic.oup.com/mnras/article/528/4/6193/7603392 by Deutsches Elektronen Synchrotron DESY user on 18 December 2024

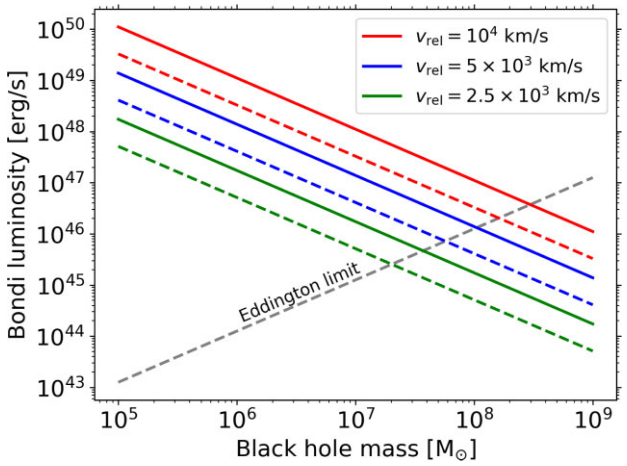

Figure 11. Bondi luminosity due to free-fall accretion of the collision product on to a black hole for different collision velocities $v_{\rm rel}$, as a function of black hole mass. The solid line is for the decelerating peak expansion speed (*Case 2: decelerating expansion*, Section 4.2.2) and dashed lines for the non-decelerating expansion speed (*Case 1: no-decelerating expansion*, Section 4.2.1). The grey dashed diagonal line indicates the Eddington luminosity.

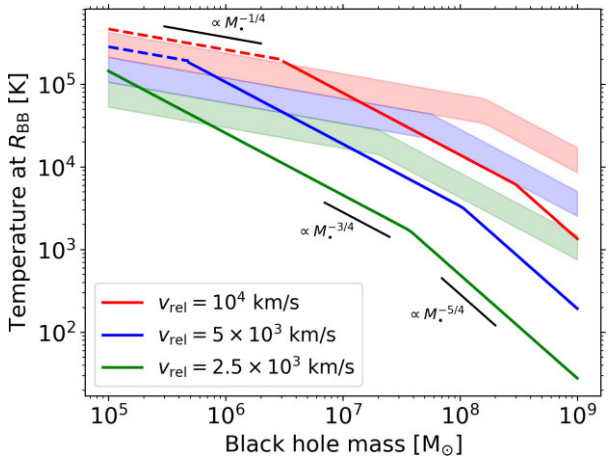

Figure 12. Temperature from the Eddington-limited Bondi luminosity at the onset of the accretion of the collision product on to a black hole for different collision velocities $v_{\rm rel}$, as a function of black hole mass. As before in Fig. 10, the lines show the case where the cloud undergoes a non-decelerating expansion up to 0.5 d, followed by a deceleration of the outer edge like $t^{-1/3}$ at 0.5 d since collision due to interactions with a background medium, using equations (2)–(7). The diagonal bars indicate the range of $\tau_{\rm BH}$ when the entire gas cloud expands without being decelerated with the peak expansion speed of (3–6) $\times$ $v_{\rm rel}$. The power laws are analytically derived in equations (18) ($\propto M_\bullet^{-1/4}$) and (27) ($\propto M_\bullet^{-3/4}$ and $\propto M_\bullet^{-5/4}$).

on $M_\bullet$ and $v_{\rm vel}$ as equations (18) and (20), because of the different expression for $\tau_{\rm BH}$, $T_{\rm Bondi}(t = \tau_{\rm BH})$ is written differently,

$$T_{\rm Bondi}(t = \tau_{\rm BH}) \simeq \begin{cases} 8 \times 10^4\,{\rm K} \left(\frac{M_\bullet}{10^7\,{\rm M}_\odot}\right)^{-3/4} \left(\frac{v_{\rm rel}}{10^4\,{\rm km\,s^{-1}}}\right)^{2.1} \left(\frac{b/R_\star+5}{5}\right)^{-6}, & \text{for } L = L_{\rm Edd}, \\ 6 \times 10^3\,{\rm K} \left(\frac{\epsilon}{0.1}\right)^{1/4} \left(\frac{M_\bullet}{10^7\,{\rm M}_\odot}\right)^{-5/4} \left(\frac{v_{\rm rel}}{10^4\,{\rm km\,s^{-1}}}\right)^{2.8} \left(\frac{b/R_\star+5}{5}\right)^{-6}, & \text{for } L = L_{\rm Bondi}. \end{cases} \quad (27)$$

We compare $T_{\rm Bondi}$ at the onset of the accretion-drive burst (so $T_{\rm Bondi}$ at $t = \tau_{\rm BH}$) in Fig. 12 between the non-decelerating expansion case (thick bars) and the decelerating expansion case (lines). For low-mass black holes, $T_{\rm Bondi}$ is quite similar, e.g. 10^5 K for $M_\bullet = 10^5$–10^6 M$_\odot$. However, because of a steeper decline for the decelerating expansion case ($T_{\rm Bondi} \propto M_\bullet^{-3/4} - M_\bullet^{-5/4}$, equation 27) than for the no-decelerating expansion case ($T_{\rm Bondi} \propto M_\bullet^{-1/4} - M_\bullet^{-3/4}$, equations 19 and 21), $T_{\rm Bondi}$ for the decelerating expansion case is generally lower for high-mass BHs: for $M_\bullet = 10^9$ M$_\odot$, $T_{\rm Bondi} \simeq 10$–10^3 K for the decelerating expansion case whereas $T_{\rm Bondi} \simeq 10^3$–$10^4$ K for the no-decelerating expansion case.

For the decelerating expansion case, the Bondi radius increases faster,

$$\frac{R_{\rm Bondi}}{R_{\rm peak}} \propto t^{4/3}, \quad (28)$$

which leads to a smaller $\tau_{\rm capture}$,

$$\tau_{\rm capture} \simeq 11\,{\rm d} \left(\frac{M_\bullet}{10^7\,{\rm M}_\odot}\right)^{3/4} \left(\frac{v_{\rm rel}}{10^4\,{\rm km\,s^{-1}}}\right)^{-2.5} \left(\frac{b/R_\star+5}{5}\right)^{-3}. \quad (29)$$

The duration of the accretion process would be the same as equation (24).

4.2.3 *Astrophysical implication for black holes*

The possibility of the accretion of at least some fraction of the expanding cloud on to the SMBH in proximity can have significant implications for the growth of BHs in the cosmic landscape. While several mechanisms for massive BH formation have been proposed, the precise mechanism for growing BH seeds at extremely high redshifts remains uncertain (see for reviews Colpi & Dotti 2011; Inayoshi, Visbal & Haiman 2020). The proposed mechanisms include rapid growth of the remnants of the Population III stars via super-Eddington accretion (e.g. Haiman & Loeb 2001; Volonteri & Rees 2005; Lupi et al. 2016; Ryu et al. 2016; Sassano et al. 2023), the direct collapse of supermassive self-gravitating objects (e.g. Omukai & Nishi 1998; Yoshida, Omukai & Hernquist 2008; Zwick et al. 2023), and growth of BHs in a runaway process (e.g. Devecchi et al. 2012; Stone, Küpper & Ostriker 2017; Tagawa, Haiman & Kocsis 2020; Rizzuto et al. 2023). In principle, as long as a BH is more massive than colliding stars, the velocity of stars around the BH can be large enough that stellar collisions can be disruptive. Hence, the accretion of gas produced in stellar collisions on to a nearby BH can provide another venue for the growth of stellar-mass BHs to massive BHs, in particular see BHs at high redshift.

However, disruptive collisions are not the only growth mechanism for BHs in stellar-dense environments. We show in Fig. 13 the regions around BHs in which several events possibly contributing to their growth, i.e. disruptive collisions, tidal disruption events, BH–star collisions, and direct captures by BHs, can occur. When the distance from the BH is less than a few times greater than the Schwarzschild radius $r_{\rm Sch} = 2GM_\bullet/c^2$ (dubbed 'direct capture' radius), the star would directly fall into the BH (e.g. $r < 2r_{\rm Sch}$ for parabolic orbits). If the closest approach distance between the BH and a star is smaller than the stellar radius, $r \lesssim R_\star$, they collide, during which the BH would gravitationally capture a fraction of the star and accrete. When a star orbits at a distance greater than both the stellar radius and the direct capture radius, and smaller than the so-called tidal radius, $r_{\rm t} = (M_\bullet/M_\star)^{1/3} R_\star$, very strong BH's tidal forces disrupt the star, creating debris, some of which would end up accreting on to the BH. This event is called tidal disruption event (Hills 1988; Rees 1988). Finally, the region for disruptive collisions between giants may be

Downloaded from https://academic.oup.com/mnras/article/528/4/6193/7603392 by Deutsches Elektronen Synchrotron DESY user on 18 December 2024

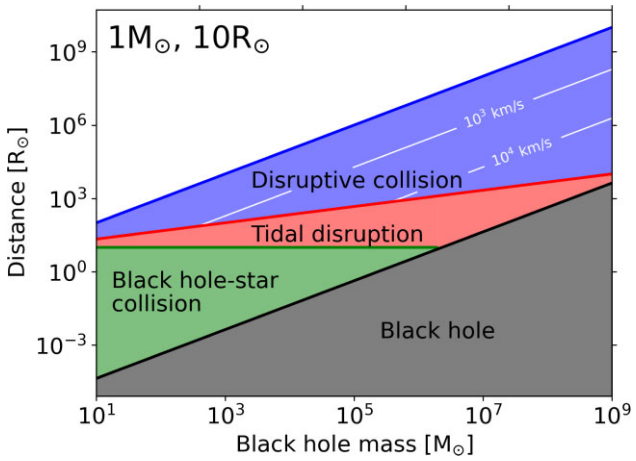

Figure 13. Parameter space for disruptive events of a giant with $M_\star = 1\,M_\odot$ and $R_\star = 10\,R_\odot$ in terms of the distance from the BH for varying BH masses. The region dubbed 'Black hole' is defined by the Schwarzschild radius, $r_{\rm Sch} = 2GM_\bullet/c^2$. If the pericentre distance of a star is smaller than a few times outside $r_{\rm Sch}$, the star would be directly captured by the black hole. If the separation is smaller than the stellar radius, they would collide ('black hole–star collision'). When the pericentre distance is smaller than the tidal radius $r \leq r_{\rm t} = (M_\bullet/M_\star)^{1/3}R_\star$, stars are tidally destroyed by the BH ('tidal disruption'). Finally, disruptive collisions happen between the distance at which the Keplerian velocity is greater than the stellar escape velocity, $r \leq r_{\rm collision} = (M_\bullet/M_\star)R_\star$ and the tidal radius $r \leq r_{\rm t}$. The white diagonal lines in the region for disruptive collisions correspond to the collision velocity for given BH mass and radius.

characterized by the two distances, the distance within which the Keplerian velocity around the BH exceeds the stellar escape speed, $r_{\rm collision} = (M_\bullet/M_\star)R_\star$ and the tidal radius.

As shown in Fig. 13, all four star destroying events can contribute to the growth of stellar-mass and intermediate-mass BHs. However, for SMBHs with $r_{\rm Sch} > R_\star$, only three events, namely, disruptive collisions, tidal disruptions, and direct captures, can feed the BHs. For very massive BHs (e.g. $M_\bullet > 10^9\,M_\odot$), disruptive collisions would be the dominant and likely only observable transient among those considered here that lead to the mass growth of the BHs (see Amaro Seoane 2023a).

This has an interesting implication for the detection of dormant BHs. TDEs have been considered a unique signpost for the existence of dormant SMBHs. However, because there is a maximum BH mass capable of disrupting stars, $M_\bullet$ at which $r_{\rm t}$ equals to the direct capture radius, TDEs cannot be used to detect very massive quiescent black holes. However, disruptive stellar collisions can occur near BHs at all mass scales, which would make these events *a promising tool to probe the existence of very massive dormant BHs* which cannot be probed by other transients. In particular, if the luminosity due to the interaction of the collision product with the BH is Eddington limited, an inference of the BH mass would potentially be possible from the observed radiated light curve.

Which type of the events is dominant at different mass ranges would depend on the stellar density, the accretion efficiency, and occurrence rates, which is beyond the scope of our paper. We will examine this aspect in more detail in our future work.

4.3 Particle acceleration

In this work, we have conducted numerical hydrodynamical simulations that confirm, following stellar collision event, the formation of strong shocks. These shocks arise due to the high velocity of the outflow, and its impact with the surrounding ISM in the galactic nucleus environment. These shock waves subsequently compress and heat the surrounding ISM gas.

The shocks formed in these stellar collisions provide an environment highly conducive to efficient particle acceleration. As particles interact with the turbulent magnetic fields expected close to the shock front, they can gain a significant fraction of the free energy available from the differential flow speeds (in the shock's rest frame, the upstream towards the shock with velocity V and the downstream moves away from the shock at velocity $V/4$). This process of diffusive particle acceleration at shocks, an example of first-order *Fermi* acceleration, is expected to result in the generation of a power-law spectrum of non-thermal particles up to very high energies (Bell 1978; Blandford & Ostriker 1978).

A fraction of the energy in the accelerated particle population produced by stellar collisions will subsequently be radiated via non-thermal emission through various energy loss processes (see Matthews, Bell & Blundell 2020; Orlando et al. 2021, for review in the context of active galactic nucleus jets and supernovae, respectively). For instance, the accelerated electrons will produce synchrotron radiation as they spiral around the magnetic fields also generated during the collision. This emission is expected to be detectable in the radio, and potentially the X-ray, bands. In addition, the interaction between accelerated protons and the surrounding gas can generate gamma-ray emission through processes like inelastic proton–proton collisions.

The non-thermal radiation emitted by the accelerated particles produced in stellar collisions offers valuable diagnostics into the physical processes at play during violent stellar collision events. By analysing the observed non-thermal radiation, we can gain a clearer understanding of shock front environment. Ultimately, these insights will elucidate on the dynamics of the collision itself. Our numerical hydrodynamics simulations, coupled with theoretical estimates for the production of non-thermal particles not included in our numerical description, can provide insights into particle acceleration in stellar collisions. This will be addressed elsewhere in a separate work.

4.4 Destructive collisions between different types of stars

Although we only consider black hole-driven disruptive collisions (BDCs) between equal-mass $1\,M_\odot$ giants, there could be a variety of BDCs involving various types of stars. The total radiated energy, luminosity, and temperature of BDCs would be affected by various factors, including the relative size and mass of the colliding stars.

It is essential to convert the collision kinetic energy into radiation energy for generating bright flares. For efficient energy conversion, one important requirement is a large contact area at collision. On the one hand, when two stars with two significantly different radii collide (e.g. main-sequence and giant) at high velocity, even if the impact parameter is small, the smaller star would simply penetrate through the fluffy envelope of the larger star. On the other hand, for collisions involving stars with comparable sizes, the dependence of luminosity on the radii of the two colliding stars may not be so simple because how strong shocks are created at collision and how rapidly photons escape after collision would be determined by several factors, such as the temperature and density of the envelop of the star before collision and those of the gas cloud after collision. At least, our simulations suggest that collisions involving larger giants are brighter because of stronger collision shocks over a wider cross-section (see Figs 9 and A1). In addition, the thermodynamic properties and chemical elements of the gas cloud would affect the spectra of the flare (Dessart et al. 2024).

Downloaded from https://academic.oup.com/mnras/article/528/4/6193/7603392 by Deutsches Elektronen Synchrotron DESY user on 18 December 2024

Another important factor that determines the collision outcome and the amount of radiated energy is the masses of the colliding stars. For the cases where at least the envelopes of the stars are completely destroyed due to collision, the total energy radiated away would be limited by the total mass of the envelopes. However, it is also possible that only one of the two colliding stars is completely destroyed. For such cases, while the total energy radiated away due to the collision would be limited by the mass of the star that is destroyed, the relatively intact star may play a role as an extra energy source that may affect the long-term evolution of the light curves. In addition, unlike the cases considered in this paper, the radiation would be highly asymmetric.

Taking all these factors into account, flares due to BDCs would generally be brighter when two stars with larger masses and comparable sizes collide at a higher velocity with a smaller impact parameter. However, due to the shorter lifetime and lower number density of more massive stars, the collision rates would be generally smaller.

5 CONCLUSION AND SUMMARY

In this work, we investigate the hydrodynamics of high-velocity collisions between giants in galactic nuclei and their observational signatures using two state-of-the-art codes, the 3D moving-mesh hydrodynamics code AREPO and the 1D stellar evolution code MESA. The initial conditions of our simulations involved two identical $1\,M_\odot$ giants with different radii, initial relative speeds, and impact parameters. This work complements to the analytical calculations presented by Amaro Seoane (2023b), which is generally consistent with each other. We improve the estimates of the events' observables by accurately taking into account the realistic stellar internal structure and non-linear hydrodynamics effects.

When two stars collide with exceedingly large kinetic energy, very strong shocks are created along the contact surface. The envelope of the two giants are fully destroyed and merged into an homologously, quasi-spherically, and supersonically expanding gas cloud. The maximum expansion speed of the cloud is larger than the initial relative velocity of the stars by a factor of 3–6. The expansion speed at a given mass coordinate stays the same, but the outer edge of the cloud slows down because of the interaction with the background medium. As it expands, the overall level of its density and temperature drops following a power law of $\propto t^{-3}$ and $\propto t^{-1}$, respectively, becoming optically thin within a few hundred days. At any given time of evolution up to 30 d, the density and temperature of the inner regions of the cloud remain relatively constant, rapidly decaying towards the outer edge, following a power law: $\rho(r) \propto r^{-8} - r^{-12}$ and $T(r) \propto r^{-1} - r^{-2}$. These quantities exhibit weak dependencies on the stellar radius within 10–100 $R_\odot$ and the impact parameter within $b \simeq 0.4\,R_\odot$. But the dependence on the collision velocity is relatively strong. We provide fitting formulae for the average cloud density, temperature, maximum expansion speed, and optical depth (equations 2–7), which would be useful for analytical estimates for these high-velocity stellar collisions.

One of the key findings of our study is to numerically estimate the amount of radiation energy converted from the initial kinetic energy, which plays a crucial role in determining the observable properties of the collisions. The overall trend of the conversion efficiency, defined as the ratio of the converted radiation energy to the initial kinetic energy, is such that it peaks at $\gtrsim$0.1 at collision, decays to 10^{-4} to 10^{-2} within 10 d, and then gradually increases. The efficiency reaches 10^{-2} to 10^{-1} in 1 month since the collision. But its magnitude depends on various factors, including the stellar radius, impact parameter, and collision velocity. More specifically, a collision between larger stars colliding at a higher speed with a smaller impact parameter tends to result in greater conversion efficiency.

We estimate the luminosity, the blackbody radius, and the blackbody temperature, using the converted radiation energy and local cooling time within the gas cloud. The peak luminosity can reach values exceeding $10^{42}\,\mathrm{erg\,s^{-1}}$ and exhibits the similar dependence wtih the conversion efficiency. Over time, the luminosity decays following a power law of $t^{-0.8}$ at early times and $t^{-0.4}$ after 10 d since collision. The blackbody radius increases almost linearly with time ($\propto t^{0.8}$), while the temperature decreases, following a power law of $t^{-0.5} - t^{-0.6}$. The collision events would initially produce bursts of extreme UV ($\simeq$10 eV) gradually shifting to optical ($\simeq$0.1eV), with temporal evolution spanning from days to weeks. These events can be observed by ongoing [e.g. Zwicky Transient Facility (ZTF), Bellm et al. 2019[6] and The All Sky Automated Survey for SuperNovae (ASSA-SN), Kochanek et al. 2017[7]] and future [e.g. Vera C. Rubin Observatory (LSST), Ivezić et al. 2019[8] and Ultraviolet Transient Astronomy Satellite (ULTRASAT), Shvartzvald et al. 2023[9]] surveys.More detailed radiation transport calculations will be carried out in our follow-up project, with which the detection rate for each survey will be estimated.

In addition to the burst resulting from the stellar collision itself, a subsequent burst occurs due to the accretion of the gas cloud on to the SMBH in the galactic centre in $5(M_\bullet/10^7\,M_\odot)$ d for $v_{\rm rel} = 10^4\,\mathrm{km\,s^{-1}}$ since collision. Assuming Bondi accretion, the accretion luminosity can easily exceed the Eddington limit as well as the luminosity from the stellar collision. Because the Bondi radius expands faster than the gas cloud, the entire cloud would be gravitationally captured in the black holes's potential in $11(M_\bullet/10^7\,M_\odot)^{3/4}$ d and subsequently accrete on to the black hole. It would take $\lesssim 9(M_\bullet/10^7\,M_\odot)^{-1}$ yr if the entire cloud was accreted. Therefore, the overall luminosity curve would include a peak from the collision event, followed by a rise to the Eddington luminosity. This heightened luminosity can be sustained for up to 10 yr.

Although the estimate of the time-scales and luminosity due to gas–black hole interactions are still of the order-of-magnitude level, this aspect indicates very important implications. The possibility of the gas accretion on to the black hole at all mass scales in proximity subsequently after the collision suggests that the collision can provide another mechanism for black hole growth. Tidal disruption events have been proposed as a tool to detect dormant black holes, mostly up to $10^8\,M_\odot$. However, because disruptive stellar collisions can occur near very massive dormant ones ($>10^9\,M_\odot$), such collisions can be a potentially promising tool to probe the existence of very massive dormant black holes.

Finally, we demonstrate the conversion of kinetic energy into radiation energy, providing insights into the efficiency of particle acceleration in these collisions. The resulting bursts of UV and optical emission indicate the generation of high-energy particles, highlighting the importance of particle acceleration processes in understanding the observational signatures of such events.

While this study, to our knowledge, is the first detailed hydrodynamics calculations of high-velocity disruptive collisions between giants, there are a few caveats in our modelling that will be improved in our future work. First, the assumption for local thermodynamic

[6] https://www.ztf.caltech.edu
[7] https://www.astronomy.ohio-state.edu/asassn
[8] https://www.lsst.org
[9] https://www.weizmann.ac.il/ultrasat

Downloaded from https://academic.oup.com/mnras/article/528/4/6193/7603392 by Deutsches Elektronen Synchrotron DESY user on 18 December 2024

equilibrium is only valid for optically thick gas. This means the evolution of the collision product at early times is accurate, but as the gas cloud becomes optically thin, our treatment of radiation pressure becomes inaccurate. As remarked in Section 3.5, this would affect the shape of the light curves at late times. We will perform detailed non-equilibrium radiation transport calculations for the late-time evolution in our follow-up project using our hydrodynamics calculations at early times when our assumption for local thermodynamic equilibrium is valid. This will significantly improve the light-curve modelling. Secondly, there are several physical impacts that we have not considered yet, such as magnetic fields, recombination, and the existence of non-thermal particles. Using the machinery that we built for this work, we will explore their impacts in a series of studies dedicated to investigating the impact of each physics.

The high-velocity disruptive collisions will offer insights into many astrophysical aspects that cannot be provided by other transients, such as the stellar dynamics and potential particle acceleration in galactic nuclei and globular clusters, black hole growth, and detection of dormant black holes.

ACKNOWLEDGEMENTS

The authors are grateful to the anonymous referee for constructive comments and suggestions. TR is grateful to Luc Dessart and Re'em Sari for constructive comments on the paper, Hans-Thomas Janka for fruitful discussions for similarities and dissimilarities of these events with core-collapse supernovae, and Ruggero Valli for providing an MESA input file for creating the giants used for the simulations. This research project was conducted using computational resources (and/or scientific computing services) at the Max Planck Computing and Data Facility. The authors gratefully acknowledge the scientific support and HPC resources provided by the Erlangen National High Performance Computing Center (NHR@FAU) of the Friedrich-Alexander-Universität Erlangen-Nürnberg (FAU) under the NHR project b166ea10. NHR funding is provided by federal and Bavarian state authorities. NHR@FAU hardware is partially funded by the German Research Foundation (DFG) – 440719683. In addition, some of the simulations were performed on the national supercomputer Hawk at the High Performance Computing Center Stuttgart (HLRS) under the grant number 44232. PAS acknowledges the funds from the 'European Union NextGenerationEU/PRTR', Programa de Planes Complementarios I+D+I (ref. ASFAE/2022/014).

DATA AVAILABILITY

Any data used in this analysis are available on reasonable request from the corresponding author.

REFERENCES

Alexander T., Hopman C., 2009, ApJ, 697, 1861
Amaro Seoane P., 2023a, preprint (arXiv:2307.10330)
Amaro Seoane P., 2023b, ApJ, 947, 8
Bahcall J. N., Wolf R. A., 1976, ApJ, 209, 214
Balberg S., Yassur G., 2023, ApJ, 952, 149
Balberg S., Sari R., Loeb A., 2013, MNRAS, 434, L26
Begelman M. C., 1979, MNRAS, 187, 237
Bell A. R., 1978, MNRAS, 182, 147
Bellm E. C. et al., 2019, PASP, 131, 018002
Benz W., Hills J. G., 1987, ApJ, 323, 614
Benz W., Hills J. G., 1992, ApJ, 389, 546
Blandford R. D., Ostriker J. P., 1978, ApJ, 221, L29
Bondi H., 1952, MNRAS, 112, 195
Bondi H., Hoyle F., 1944, MNRAS, 104, 273
Choi J., Dotter A., Conroy C., Cantiello M., Paxton B., Johnson B. D., 2016, ApJ, 823, 102
Colpi M., Dotti M., 2011, Adv. Sci. Lett., 4, 181
Dale J. E., Davies M. B., 2006, MNRAS, 366, 1424
Dessart L., Ryu T., Amaro Seoane P., Taylor A. M., 2024, A&A, 682, A58
Devecchi B., Volonteri M., Rossi E. M., Colpi M., Portegies Zwart S., 2012, MNRAS, 421, 1465
Freitag M., Benz W., 2005, MNRAS, 358, 1133
GRAVITY Collaboration, 2019, A&A, 625, L10
Gillessen S. et al., 2019, ApJ, 871, 126
Haiman Z., Loeb A., 2001, ApJ, 552, 459
Herwig F., 2000, A&A, 360, 952
Hillier D. J., Dessart L., 2012, MNRAS, 424, 252
Hills J. G., 1988, Nature, 331, 687
Hills J. G., Day C. A., 1976, Astrophys. Lett., 17, 87
Hut P. et al., 1992, PASP, 104, 981
Iglesias C. A., Rogers F. J., 1996, ApJ, 464, 943
Inayoshi K., Visbal E., Haiman Z., 2020, ARA&A, 58, 27
Ivezić Ž. et al., 2019, ApJ, 873, 111
Kochanek C. S. et al., 2017, PASP, 129, 104502
Lai D., Rasio F. A., Shapiro S. L., 1993, ApJ, 412, 593
Langer N., Fricke K. J., Sugimoto D., 1983, A&A, 126, 207
Ledoux W. P., 1947, ApJ, 105, 305
Lupi A., Haardt F., Dotti M., Fiacconi D., Mayer L., Madau P., 2016, MNRAS, 456, 2993
Matthews J. H., Bell A. R., Blundell K. M., 2020, New Astron. Rev., 89, 101543
Neumayer N., Seth A., Böker T., 2020, A&AR, 28, 4
Ohlmann S. T., Röpke F. K., Pakmor R., Springel V., 2017, A&A, 599, A5
Omukai K., Nishi R., 1998, ApJ, 508, 141
Orlando S., Miceli M., Ustamujic S., Tutone A., Greco E., Petruk O., Bocchino F., Peres G., 2021, New Astron., 86, 101566
Pakmor R., Springel V., Bauer A., Mocz P., Munoz D. J., Ohlmann S. T., Schaal K., Zhu C., 2016, MNRAS, 455, 1134
Paxton B., Bildsten L., Dotter A., Herwig F., Lesaffre P., Timmes F., 2011, ApJS, 192, 3
Paxton B. et al., 2013, ApJS, 208, 4
Preto M., Amaro-Seoane P., 2010, ApJ, 708, L42
Rauch K. P., 1999, ApJ, 514, 725
Rees M. J., 1988, Nature, 333, 523
Reimers D., 1975, in Problems in Stellar Atmospheres and Envelopes. Springer-Verlag, New York, p. 229
Rizzuto F. P., Naab T., Rantala A., Johansson P. H., Ostriker J. P., Stone N. C., Liao S., Irodotou D., 2023, MNRAS, 521, 2930
Rose S. C., Naoz S., Gautam A. K., Ghez A. M., Do T., Chu D., Becklin E., 2020, ApJ, 904, 113
Rose S. C., Naoz S., Sari R., Linial I., 2023, ApJ, 955, 30
Ryu T., Tanaka T. L., Perna R., Haiman Z., 2016, MNRAS, 460, 4122
Sassano F., Capelo P. R., Mayer L., Schneider R., Valiante R., 2023, MNRAS, 519, 1837
Sellgren K., McGinn M. T., Becklin E. E., Hall D. N., 1990, ApJ, 359, 112
Shvartzvald Y. et al., 2023, preprint (arXiv:2304.14482)
Springel V., 2010, MNRAS, 401, 791
Stone N. C., Küpper A. H. W., Ostriker J. P., 2017, MNRAS, 467, 4180
Tagawa H., Haiman Z., Kocsis B., 2020, ApJ, 892, 36
Volonteri M., Rees M. J., 2005, ApJ, 633, 624
Weinberger R., Springel V., Pakmor R., 2020, ApJS, 248, 32
Yoshida N., Omukai K., Hernquist L., 2008, Science, 321, 669
Zwick L., Mayer L., Haemmerlé L., Klessen R. S., 2023, MNRAS, 518, 2076

APPENDIX A: LUMINOSITY ESTIMATE

Fig. A1 show the luminosity L_2 (*top*) estimated using equation (12) and the resulting blackbody temperature $T_{\rm BB}$ (*bottom*), as a function of time measured since collision for all our models.

Downloaded from https://academic.oup.com/mnras/article/528/4/6193/7603392 by Deutsches Elektronen Synchrotron DESY user on 18 December 2024

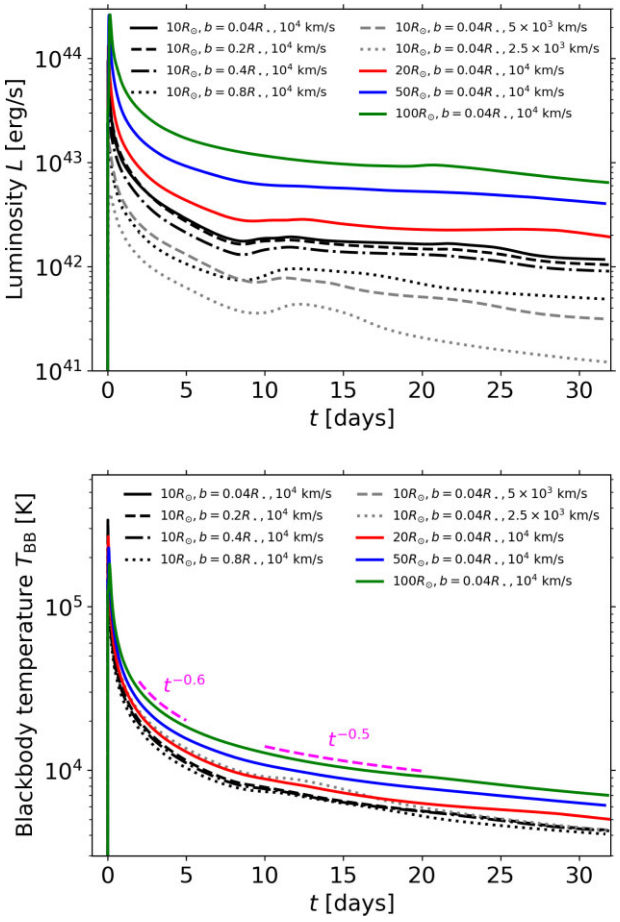

Figure A1. Bolometric luminosity L_2 (*top*) and blackbody temperature T_{BB} (*bottom*) using equations (10) and (12). As in Fig. 9, the magenta guide lines in the *bottom* panel show the power law that describes the quantity.

This paper has been typeset from a TEX/LATEX file prepared by the author.

Downloaded from https://academic.oup.com/mnras/article/528/4/6193/7603392 by Deutsches Elektronen Synchrotron DESY user on 18 December 2024

© 2024 The Author(s).
Published by Oxford University Press on behalf of Royal Astronomical Society. This is an Open Access article distributed under the terms of the Creative Commons Attribution License (https://creativecommons.org/licenses/by/4.0/), which permits unrestricted reuse, distribution, and reproduction in any medium, provided the original work is properly cited